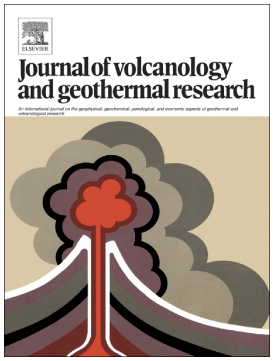

Magma storage conditions beneath a peralkaline caldera in the Main Ethiopian Rift

David J. Colby, David M. Pyle, Karen Fontijn, Tamsin A. Mather, Sebastien Nomade, Abate A. Melaku, Million A. Mengesha, Gezahegn Yirgu

PII: S0377-0273(24)00157-4

DOI: https://doi.org/10.1016/j.jvolgeores.2024.108165

Reference: VOLGEO 108165

To appear in: *Journal of Volcanology and Geothermal Research*

Received date: 9 June 2023

Revised date: 13 August 2024

Accepted date: 13 August 2024

Please cite this article as: D.J. Colby, D.M. Pyle, K. Fontijn, et al., Magma storage conditions beneath a peralkaline caldera in the Main Ethiopian Rift, *Journal of Volcanology and Geothermal Research* (2024), https://doi.org/10.1016/j.jvolgeores.2024.108165

Magma storage conditions beneath a peralkaline caldera in the Main Ethiopian Rift

David J Colby[ab*], David M Pyle[a], Karen Fontijn[c], Tamsin A Mather[a], Sebastien Nomade[d,] Abate A Melaku[e,f], Million A Mengesha[f] Gezahegn Yirgu[f]

a) *Department of Earth Sciences, University of Oxford, United Kingdom*

b) *Department of Earth Sciences, Durham University, Durham*

c) *Laboratoire G-Time, Department of Geosciences, Environment, and Society, Université libre de Bruxelles, Belgium*

d) *LSCE, UMR 8212, CEA, CNRS , Université de Versailles St-Quentin et Paris Saclay, Avenue de la Terrasse, 91190 Gif-sur-Yvette Cedex, France*

e) *School of Earth and Environmental Sciences, University of St. Andrews, United Kingdom*

f) *School of Earth Sciences, Addis Ababa University, Ethiopia*

*david.j.colby@durham.ac.uk

Abstract

The numerous volcanic centres in the Main Ethiopian Rift (MER) present significant but poorly understood hazards to local populations. The MER is also an important site to gain insights into tectonic processes as it captures the transition from continental rifting (to the south) to incipient seafloor spreading (to the north). Peralkaline magmas account for around 90% of the volcanic products found in the MER. Determining the conditions under which these magmas evolve is critical to understanding rift-related volcanism and its associated hazards. Corbetti Caldera has an extensive record of large-scale, predominantly aphyric, peralkaline rhyolite eruptions. However, little is known about the mafic magmas from which these highly differentiated melts have evolved. Here we present data from the only basaltic deposit found within the caldera, coupled with whole rock, glass and mineral analysis of the peralkaline products, to investigate magma storage conditions at Corbetti. We demonstrate that magma mixing played a role in the evolution of the basaltic magmas and use RhyoliteMELTS modelling to show Corbetti's peralkaline magmas likely evolved at pressures between 100 and 250 MPa, from a magma with an initial water content of 0.5 – 1 wt.%, at or below the QFM buffer. Mineral hygrometry on the sparse crystal populations corroborates the RhyoliteMELTS

modelling, suggesting that the basaltic magma had 0.1-1.2 ± 0.32 wt.% H_2O, and the peralkaline magmas an average of ~5.5 ± 1.25 wt.% H_2O. These results also match melt inclusion data for Corbetti and other peralkaline systems. We also provide new $^{40}Ar/^{39}Ar$ sanidine ages for two eruptions, a pre-caldera rhyolitic lava flow (206.7 ± 0.9 ka) and a post-caldera peralkaline ignimbrite (160 ± 0.8 ka). These results add to our understanding of the history of Corbetti and the storage conditions of peralkaline magmas within a continental rift setting and highlight the hydrous nature of Corbetti's magmas and the role that H_2O plays during explosive eruptions.

Keywords:

Peralkaline; Geochemistry; Petrology; RhyoliteMELTS; Alkali Basalt

1 Introduction

Understanding the nature of magmatic systems and the processes governing magma evolution is critical when investigating the surface expression of volcanism and unpicking signals of unrest. This is particularly true for regions such as the Main Ethiopian Rift (MER), which has multiple volcanic centres that have shown historical unrest and have erupted highly differentiated peralkaline magmas in the past (Biggs et al., 2021).

The MER is a key natural laboratory to study the evolution of peralkaline magmas due to its high density of peralkaline centres along a maturing continental rift (Ebinger, 2005). Studies investigating the nature of volcanism within the rift (Hutchison et al., 2016b; Rapprich et al., 2016; Martin-Jones et al., 2017; Fontijn et al., 2018; Tadesse et al., 2019, 2022; Colby et al., 2022) and the processes governing magma evolution in the MER (Gleeson et al., 2017; Hutchison et al., 2018; Iddon et al., 2019; Tadesse et al., 2023, 2019) have highlighted the bimodal nature of eruptive compositions and the dominance of peralkaline rhyolites (molar $(Na_2O + K_2O)/Al_2O_3 > 1$; Shand, 1927). It is generally accepted that the peralkaline products of the MER form through progressive fractional crystallisation of an alkali basalt at low pressures and reducing conditions (Scaillet and MacDonald, 2003; Di Carlo et al., 2010; Gleeson et al., 2017); while some centres also show signatures of minor crustal contamination (Peccerillo et al., 2003; Giordano et al., 2014; Hutchison et al., 2018). The compositional hiatus between 52-64 wt.% SiO_2, known as the Daly gap, is observed throughout the MER (Peccerillo *et al.*, 2003; Ronga *et al.*, 2009; Rooney *et al.*, 2012; Hutchison, *et al.*, 2016; Gleeson *et al.*, 2017; Tadesse *et al.*, 2019). This compositional gap is a poorly understood feature of magma

evolution within the MER. It has been attributed to various processes, including high silica activity between 52-64 wt.% SiO_2, resulting in fast differentiation towards rhyolitic compositions (Iddon and Edmonds, 2020; White et al., 2009) and magma mixing (Ferla and Meli, 2006); however, further investigation is required to constrain the processes governing this feature.

The peralkaline rhyolites of the MER range from comendites ($Fe/Al* = 1.33 \cdot FeOT / (Al_2O_3 – 4.4) < 1$; White et al., 2023) to pantellerites ($Fe/Al* > 1$) and are erupted both explosively and effusively from large silicic centres, usually associated with calderas (Fontijn et al., 2018), which are distributed along the rift axis (Figure 1). Eruptive products of basaltic compositions are rarely found within large silicic calderas. Basalts are generally found at off-edifice locations and appear primarily controlled by rift-related structures. For instance, the Wonji Fault belt controls the location of the Wonji Basalts at Gedemsa (Peccerillo et al., 2003) and scoria cones near Aluto (Hutchison *et al.*, 2016). Samples of basaltic eruptions have been reported from Aluto and Bora-Baricha – Tullu Moye calderas (Hutchison et al., 2016b; Tadesse et al., 2019, 2023).

1.1 Geological Setting of Corbetti Caldera

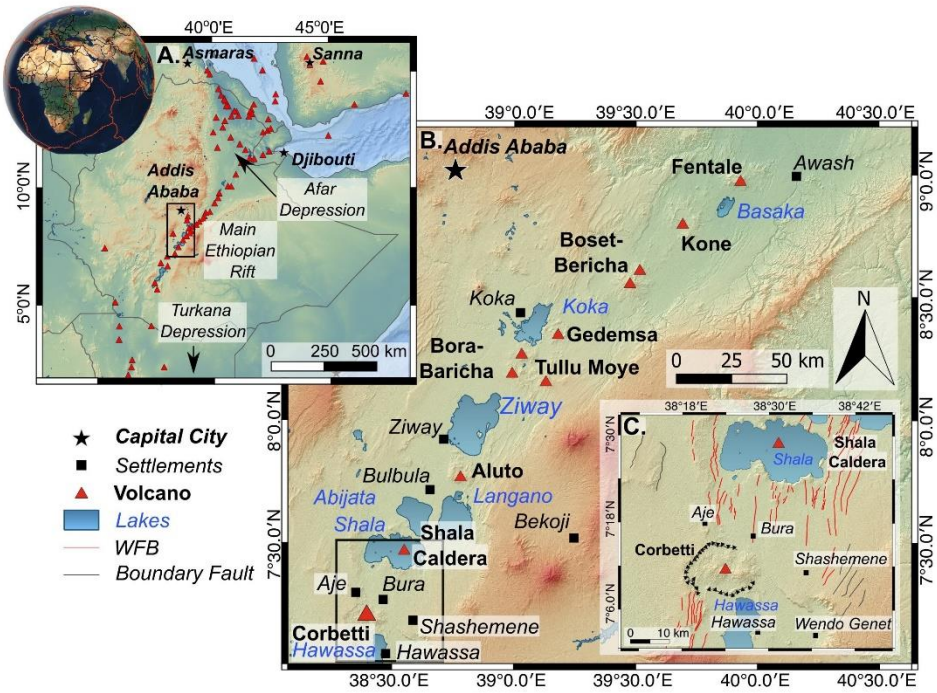

Figure 1: A) Regional map of the East African Rift, highlighting the area in B. B) Central and Southern section of the Main Ethiopian Rift, showing the location of Corbetti Caldera, and other major silicic centres. C) Overview map of Corbetti Caldera highlighting regional faults and the Wonji Fault Belt (WFB). Faults after Agostini et al. (2011).

Here we investigate one restless caldera system, Corbetti Caldera (Lloyd et al., 2018a; Lloyd et al., 2018b), a large silicic centre in the southernmost part of MER that has predominantly erupted aphyric, peralkaline rhyolites. Corbetti has followed a similar evolutionary pattern to other silicic centres in the MER (Hutchison et al., 2016b), undergoing an initial shield-building phase, followed by at least one caldera-forming eruption dated to ~182 ka and subsequent development of post-caldera edifices (Hutchison et al., 2016; Vidal et al., 2022a). Post-caldera volcanism has centred around three edifices: Artu, Urji and Chabbi (Figure 2A). Artu is heavily eroded, with little known about its eruptive history. Urji and Chabbi have both erupted geochemically similar peralkaline rhyolite magmas, with Urji dominated by pumice-cone-forming eruptions and Chabbi dominated by the eruption of large obsidian lava flows (Colby et al., 2022; Fontijn et al., 2018; Rapprich et al., 2016). An overview of the stratigraphy at Corbetti is presented in Figure 3, and the key units for this study are highlighted. Over the last 2.3 ky, Corbetti has experienced explosive and effusive eruptions, with a recurrence rate of around one eruption per 300-400 years (Colby et al., 2022; Fontijn et al., 2018). InSAR data collected between 2015 and 2020 show that steady uplift has been occurring at Corbetti at a rate of ~ 4.6 cm/yr^{-1}, interpreted as continual pressurisation of a large magmatic reservoir at around 7 km depth, is anticipated to be ongoing (Albino et al., 2022; Albino and Biggs, 2021).

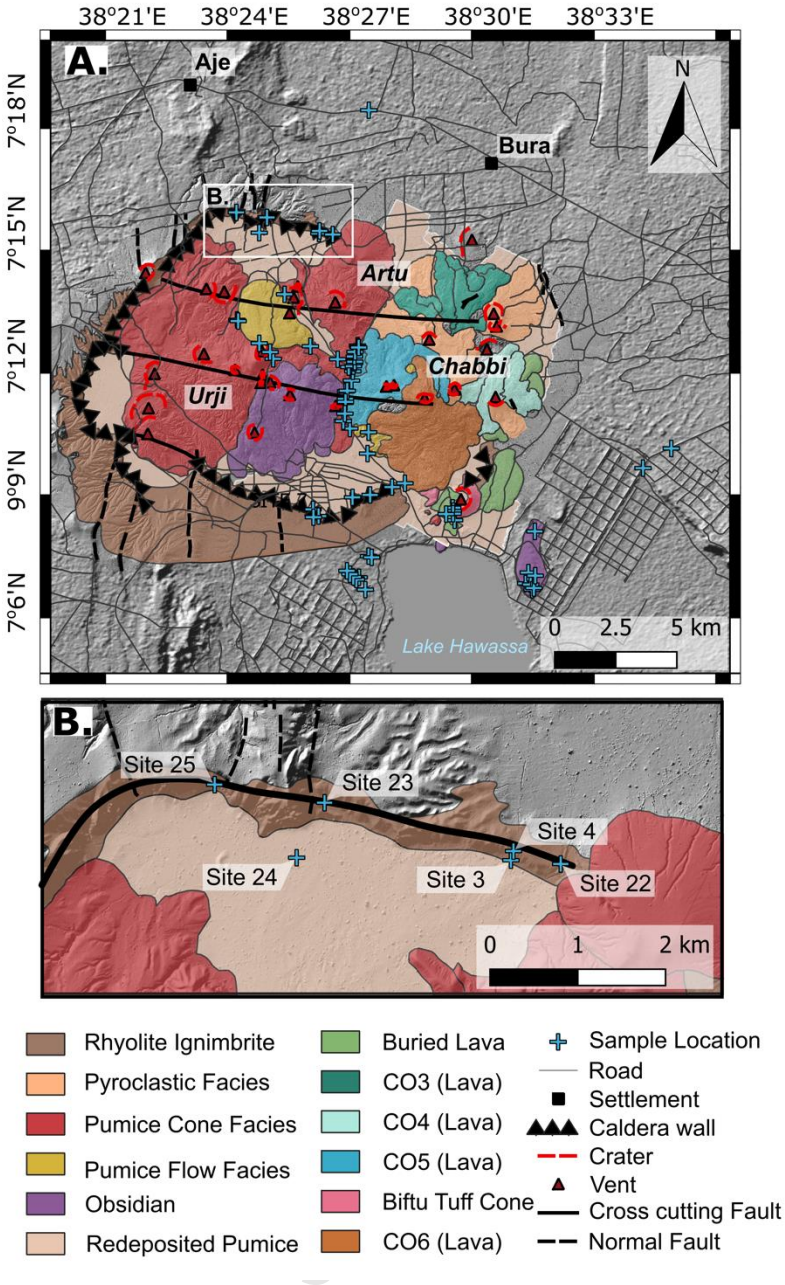

Figure 2: Geological map of Corbetti Caldera highlighting the sample locations (after Hunt, et al., 2019; Colby et al.*, 2022). B) Detail of the northern caldera walls showing sample sites of the two end-member samples analysed in this study. CO3-6 are obsidian lava flows from Chabbi*

This study seeks to understand the magma storage conditions at Corbetti Caldera . We investigate two endmember compositions, an alkali basaltic tuff and a welded peralkaline ignimbrite, to offer an insight into how Corbetti's magma likely evolved. We employ RhyoliteMELTS modelling and compare these results to petrological findings to test the

validity of using RhyoliteMELTS on peralkaline systems. We also look in detail at the only recorded basaltic eruption at Corbetti and provide insights into the magmatic processes occurring before its eruption.

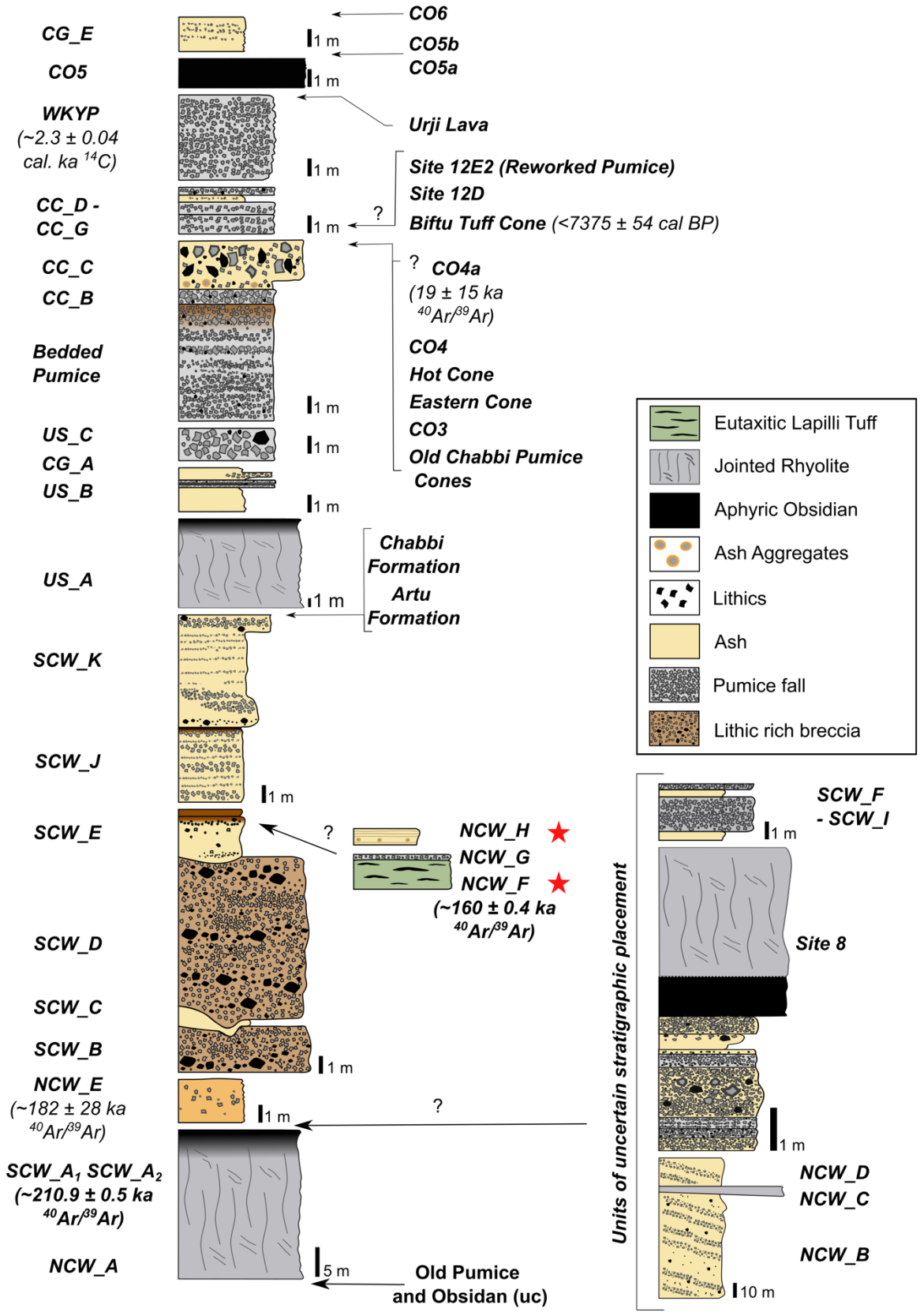

Figure 3: Composite stratigraphy of Corbetti Caldera after Colby et al. (2022) showing the range in pre-, syn-and post-caldera eruptive activity. Units that are the study's focus (NCW_F

and NCW_H) are highlighted with a red star. New dates for SCW_A2 and NCW_F are also included.

1.2 Overview of studied units.

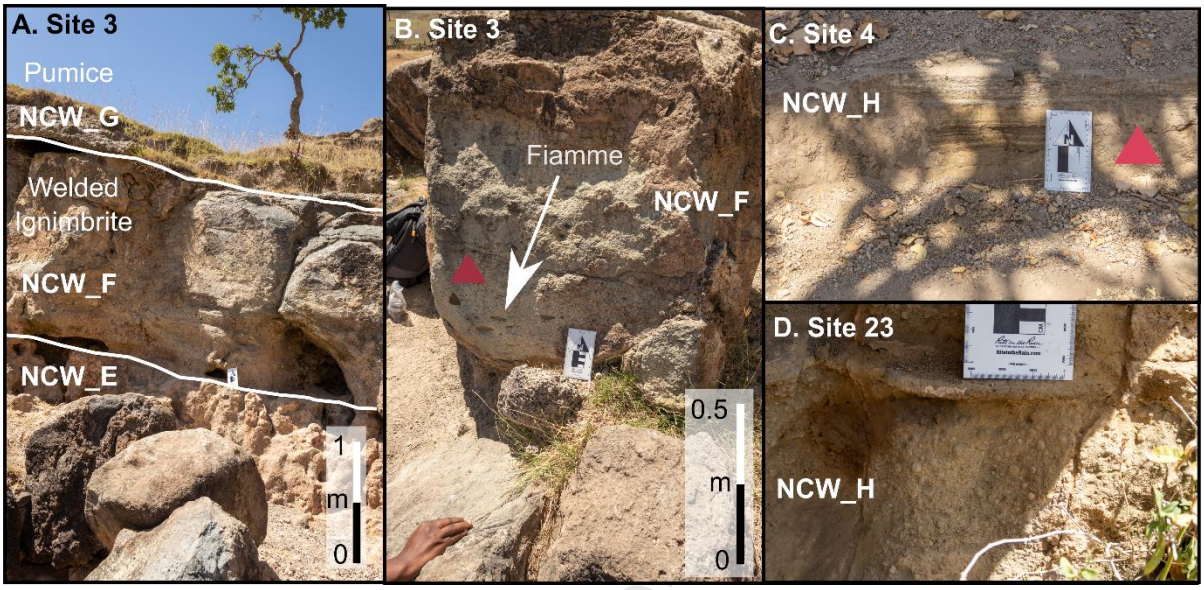

Figure 4: Field photos of deposits in north caldera walls (Site 3 & 4; Figure 2B) highlighting outcrops of the two endmembers investigated in this study a welded ignimbrite (NCW_F) and basaltic tuff (NCW_H). Adapted from Colby et al. *(2022).*

The two endmembers studied here have been previously characterised by Colby et al. (2022). NCW_H is a basaltic, ash aggregate bearing, stratified ash-rich tuff found within the northern caldera wall (Site 4; Figure 2B and Figure 4C & D) inferred to have been deposited by dilute pyroclastic density currents (PDCs). The dilute nature of the deposit and the presence of ash aggregates suggests it may be of phreatomagmatic origin. This unit is only exposed in two locations in the northern caldera walls (Figure 2B). Hereafter, the unit is referred to as the 'Basaltic Tuff'. NCW_F underlies the Basaltic Tuff (Site 3; Figure 2B, 4A & B) and is a massive green eutaxitic lapilli tuff deposited by a PDC, hereafter referred to as the 'welded ignimbrite'. Currently, this unit has only been reported at a single locality (Figure 2B). Both of these units overlie the ignimbrite associated with the 182-ka caldera-forming eruption. These two endmember compositions form the basis for our petrological investigation and comparison with the results of our RhyoliteMELTS simulations.

In addition to these units, only a few deposits at Corbetti contain crystalline material. Phenocrysts are almost exclusively restricted to large rhyolitic lava flows, which comprise significant parts of the northern and southern caldera walls, the ignimbrite associated with the

caldera-forming eruption (NCW_E) and sparse crystalline portions of obsidian lavas (Colby et al., 2022). None of these latter units returned suitable glass and mineral data for thermometry and hygrometry analysis.

2 Methods

2.1 Whole Rock, Glass and Mineral Geochemistry

Glass and mineral major element compositions were analysed by a Cameca SXFive Electron Probe Micro-Analyser at the Department of Earth Sciences, Oxford, fitted with five spectrometers: PET (K, Ti), TAP (Na, Mg), LPET (Ca, P, Zr), TAP (Si, Al) and LLIF (Mn, Fe). Beam conditions were set at 15 kV, 10 nA, with a beam size of 10 μm for both glass and mineral phases. Analysis of mineral phases in the enclave found in sample NCW_F required a smaller beam size of 5 μm. The probe was calibrated on in house primary standards (Si, Al and Na on Albite, Ca on Wollastonite, Mn on Mn, Fe on Fayalite, K on Sanidine, Ti on Rutile, Mg on MgO, P on Durango Apatite). Count times on peak for elements were between 30 and 50 seconds in general and 12 seconds for Na. Backgrounds were collected for half the time either side of the peak. Alkali elements were measured first to minimise Na loss. Analytical totals below 97 wt.% for the alkali basalt glass and below 95 wt.% for the peralkaline ignimbrite were rejected. Glass compositions were normalised to an anhydrous composition. Lower totals for the peralkaline ignimbrite are likely due to high water contents in the glass. The measured values of secondary glass standards agreed with the ideal values. Mineral data consistently recorded totals better than 99 wt.%. Any mineral analysis with totals below 99 wt.% were rejected. Full details can be found in Supplementary files A1and C

For whole rock analysis, samples were cleaned, oven-dried, crushed, and powered in an agate ball mill and analysed using ICP-OES for major elements and ICP-MS for trace elements at Activation Laboratories, Canada (Details and data presented in Colby et al., 2022).

2.2 $^{87}Sr/^{86}Sr$ Isotope Analysis

Strontium isotope ratios were determined for 10 samples representing a range of silicic pre-, syn- and post-caldera eruptions, including the two endmembers considered here. Details of these units can be found in the supplementary information. Ratios were determined using the NU Plasma II MC-ICP-MS at the Laboratoire G-Time, Université libre de Bruxelles (Brussels, Belgium). Two measurements were taken for each sample, and an average was reported. The average values have a 2SD of less than 0.000041. Samples were analysed alongside secondary

standard NBS987 (Weis et al., 2006) and an in-house carbonate sample. Measured values for the standards were within 0.001% of expected values (See supplementary file C for details).

2.3 $^{40}Ar/^{39}Ar$ Dating

The $^{40}Ar/^{39}Ar$ ages for the units SCW_A2 and NCW_F were obtained at the Laboratoire des Sciences du Climat et de l'Environnement (CEA, CNRS UMR 8212, Gif-sur-Yvette, France) dating facility. These units were selected as they had abundant K-rich feldspars and would provide further constraints on the timing of early activity at Corbetti and the onset of post-caldera activity. Twenty to thirty K-feldspars with no visible inclusions were hand-picked, leached for 5 minutes in a 10% HF solution before being irradiated in the CLICIT facility of Oregon State University TRIGA for one hour, IRR. CO-019. The five Argon isotopes (^{40}Ar, ^{39}Ar, ^{38}Ar, ^{37}Ar and ^{36}Ar) were measured using a multicollector NGX 600 mass spectrometer equipped with 9 ATONA® amplifiers array and an electron multiplier. Peak intensity data were reduced using ArArCALC V2.4 (Koppers, 2002). Neutron fluence J factor was calculated using co-irradiated Alder Creek sanidine standard ACs-2 associated to an age of 1.1891 Ma (Niespolo et al., 2017) according to the K total decay constant of Renne et al. (2011) (λe.c. = (0.5757 ± 0.016) × 10− 10 yr^{-1} and $\lambda\beta^{-}$ = (4.9548 ± 0.013) × 10− 10 yr^{-1})). To determine this neutron flux, 14 flux monitor crystals from pits framing the samples in each irradiation disk were used. J-values measured 0.00028170 ± 0.00000020 for both samples that were irradiated to the same level. To verify the detector's linearity, mass discrimination was monitored by analysis of at least 10 air shots of various beam sizes ranging from 1.0×10^{-2} up to 5.0×10^{-2} V (1 to 5 air shots). About 15 air shots analyses are performed every day. These measurements are done automatically during the nights before and after the unknown measurements. Discrimination is calculated according to the $^{40}Ar/^{36}Ar$ ratio of 298.56 (Lee et al., 2006). Procedural blank measurements were achieved after every two to three unknowns. For a typical 5 min time, blank backgrounds are between 0.6 and 2.3×10^{-4} V for ^{40}Ar and 20 to 50 cps for ^{36}Ar (about 3.0–7 $\times 10^{-7}$ V equivalent). Full analytical data for each sample and methodology can be found in Supplementary files A3 and C respectively.

3 Results

3.1 Geochemistry and $^{87}Sr/^{86}Sr$ Ratios

The Basaltic Tuff within the northern caldera wall (NCW_H) is the only example of a deposit from a basaltic eruption so far found within the complex (Colby et al., 2022). The composition of individual glass shards is broadly homogenous; however, there is significant variation between individual shards which range from basaltic (46.3 wt.% SiO_2) to basaltic andesite (54 wt.% SiO_2) (Figures 5 & 6). In addition, obsidian lithics were also found encased in basaltic glass. These were highly silicic, ranging from 75 to 76.8 wt.% SiO_2 (Figure 5B), weakly peralkaline comendites (Peralkalinity Index = 1.01-1.13).

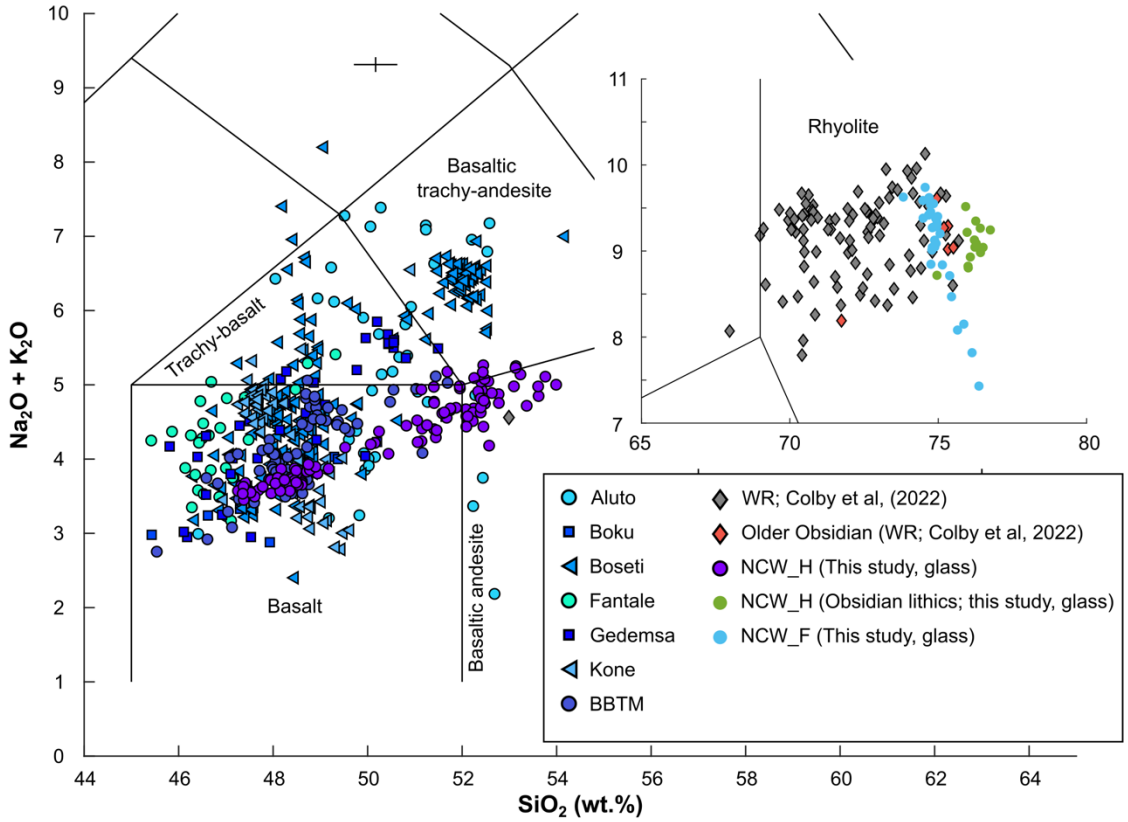

Figure 5: A) Total Alkali-Silica plot comparing the glass compositions reported here with glass (G) and whole-rock (WR) basaltic compositions reported at other calderas within the MER. Aluto; Teklemariam et al. (1996) (WR); Hutchison et al. (2016b) (WR); Fontijn et al. (2018) (G), Boku: Tadesse et al. (2019) (WR), Boset: Brotzu et al. (1980) (WR); Furman et al. (2006) (WR); Fontijn et al. (2018 (WR)), Fentale: Furman et al. (2006) (WR); Rooney et al. (2007) (WR); Giordano et al. (2014) (WR), Gedemsa: Chernet and Hart, (1999) (WR); Peccerillo et

al. (2003) (WR); Rooney et al. (2007) (WR); Giordano et al. (2014) (WR), Kone: Rooney et al. (2007) (WR); Fontijn et al. (2018) (G), BBTM: : Fontijn et al., (2018) (G); Tadesse et al. (2023) (WR). B) TAS plot (Axis the same as A) showing the composition of the obsidian lithics compared with WR peralkaline rhyolite samples from Corbetti and the glass compositions from NCW_F. Error bar is for data collected in this study.

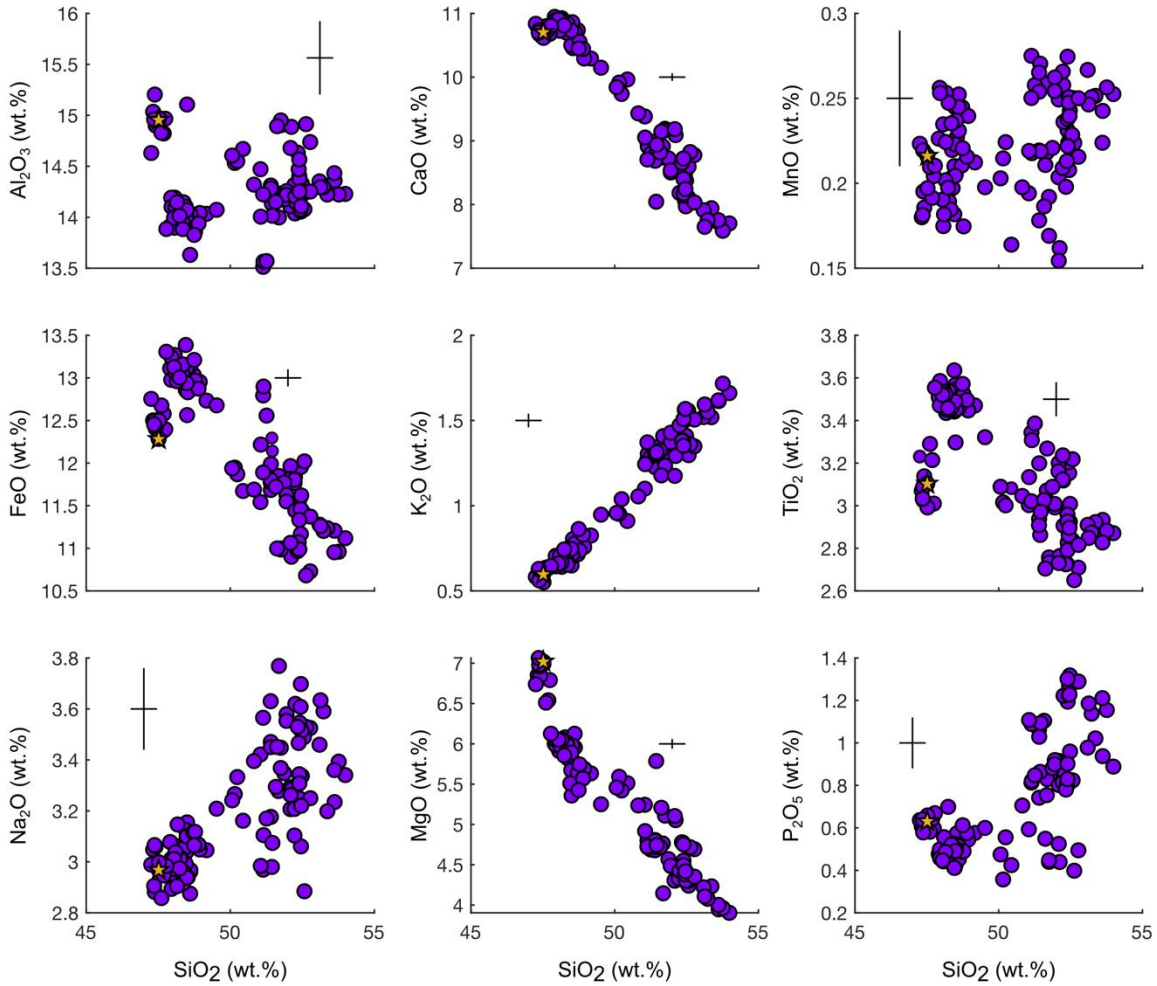

Figure 6: Harker diagrams showing the variation of basaltic glass compositions recorded within the Basaltic Tuff (NCW_H). Samples above ~50 wt.% SiO_2 show increased scatter in MnO, FeOt, TiO_2 and Na_2O. Star indicates the initial composition used for the RhyoliteMELTS modelling (see section 4).

Glass compositions from the Basaltic Tuff record a fractional crystallisation trend (progressive decrease in CaO and MgO with increasing SiO_2) which is consistent with other volcanoes within the MER (Hutchison et al., 2016b; Gleeson et al., 2017); however, there is significant scatter in the observed MnO, Na_2O, and P_2O_5 concentrations above 50 wt.% SiO_2. The cause

of this variation is unclear. We exclude analytical artefacts since there is no discernible decrease in Na_2O concentration, with decreasing analytical totals indicating that Na loss is unlikely the cause. Figure 5 shows a comparison of this new data for Corbetti with other systems across the MER. It demonstrates some heterogeneity in erupted compositions across the rift, especially with respect to total alkali content. Corbetti's basaltic compositions have a slightly lower overall alkali content; however, they are comparable with those that erupted from Aluto and Gedemsa.

Whole rock trace element geochemistry published in Colby et al. (2022) is presented in Figures 7 & 8, highlighting the incompatible trace element trends and the mean trace element composition of units normalised to primitive mantle compositions (McDonough and Sun, 1995). There is little variation between the silicic peralkaline eruptive units, especially between post-caldera deposits, making differentiation between units based on composition alone challenging (Colby et al., 2022; Fontijn et al., 2018). The peralkaline magmas show characteristic depletion with respect to the primitive mantle in Ba and Sr. Whilst most samples show the expected trends of a highly differentiated peralkaline magma, Figure 7 highlights some examples, which span several stratigraphic units, that have a lower Zr/Nb ratio. These samples also have high Zr/Hf ratios (57-72) compared with the rest of the dataset (40-52). Zr/Hf ratios are expected to remain constant through fractionation. For instance, samples from the WKYP unit show relatively constant Zr values but decreasing Nb (Figure 7).

$^{87}Sr/^{86}Sr$ isotope values for selected samples are reported in Table 1. All but one of the samples have values in the range 0.7043-0.7051, in good agreement with previous $^{87}Sr/^{86}Sr$ data for Corbetti (Rapprich et al., 2016). One sample, NCW_E, shows a more elevated isotopic signature of 0.7062 and matches the value for the caldera-forming ignimbrite reported by Rapprich et al. (2016).

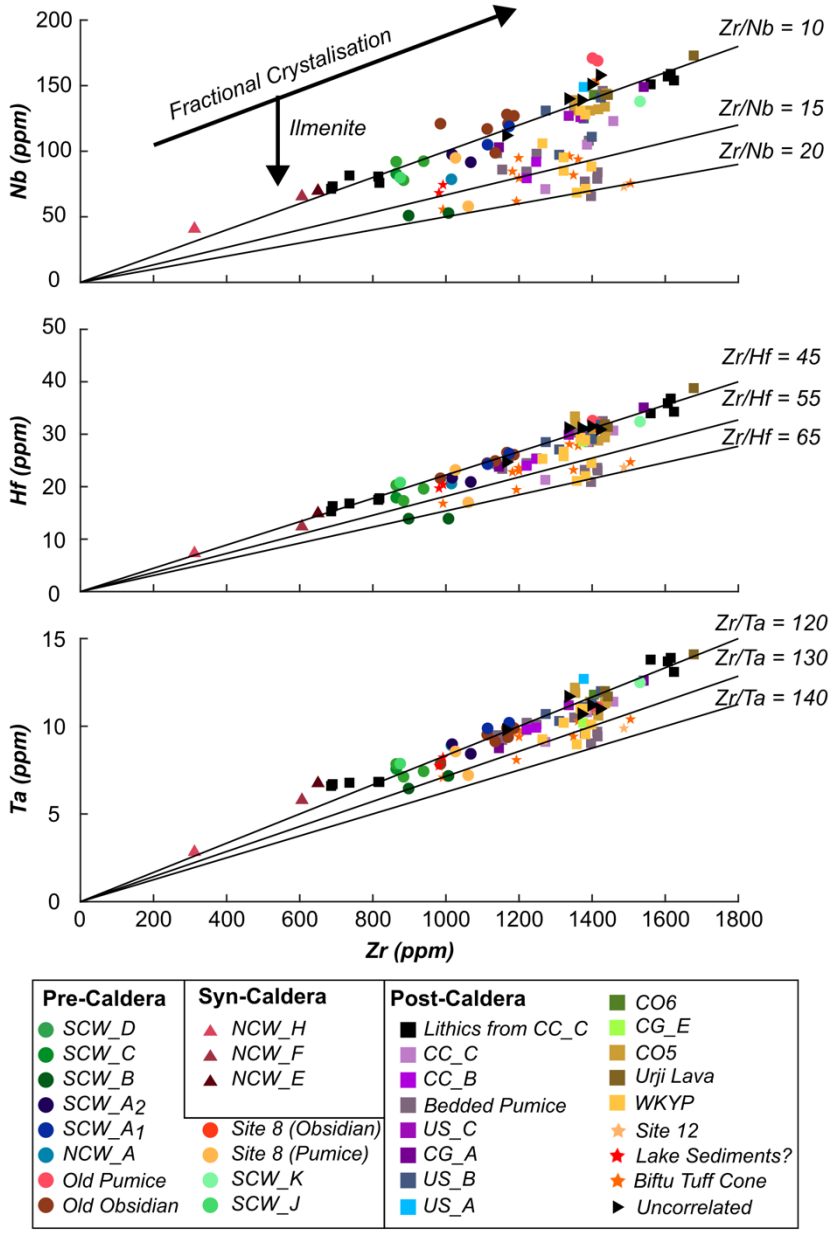

Figure 7: Selected whole-rock incompatible trace element plots which show fractional crystallisation trends (increasing incompatible elements with increasing Zr). Black lines highlight the trends of different ratios of Zr to respective elements. Some sample sets show lower-than-expected values for Nb, Hf and Ta, which may represent the crystallising of ilmenite or a cryptic phase not seen in the eruptive products.

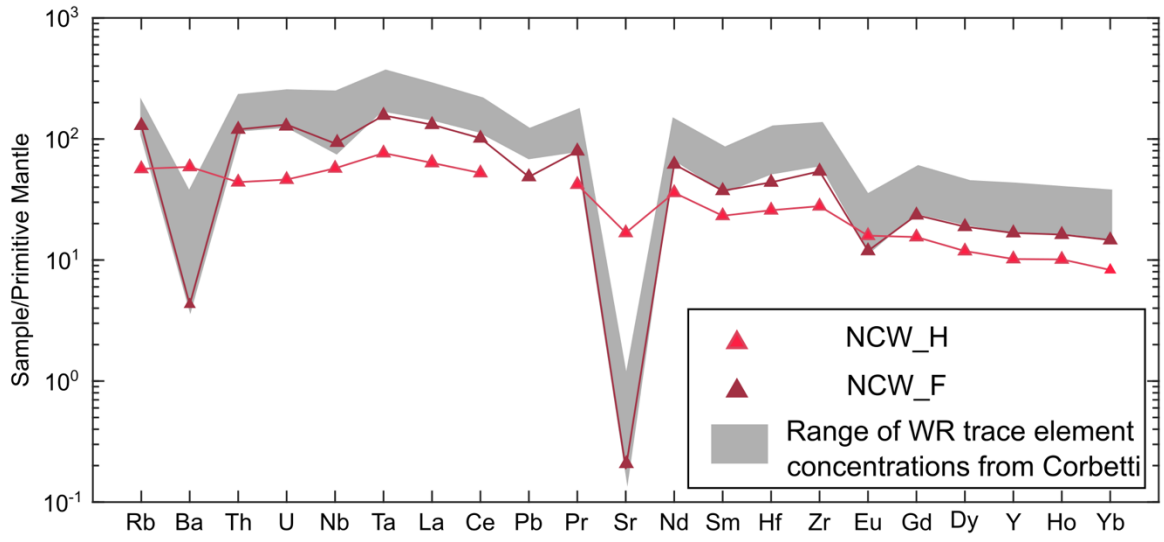

Figure 8: Spider diagrams showing the range of whole-rock trace elements for units at Corbetti (after Colby et al., 2022) normalised to the primitive mantle (McDonough and Sun, 1995). The two endmember compositions used in this study are highlighted here. NCW_H does not show a characteristic basaltic trace element trend due to the presence of rhyolitic glass and felsic minerals within the sample.

Table 1: Whole rock $^{87}Sr/^{86}Sr$ ratios for selected samples. Samples cover a range of pre-, syn- and post-caldera eruptions. Figure 2 shows the stratigraphic relationship of these units. Locations are described in Colby et al. (2022).

Correlation[1]	Material	Location[1]	Sr (ppm)	$^{87}Sr/^{86}Sr$	2SD[2]
SCW_A2	Lava	Site 7B	2	0.705029	0.000041
NCW_E	Ignimbrite	Site 2B	9	0.706223	0.000004
NCW_F	Ignimbrite	Site 3B	4	0.704972	0.000013
NCW_H	Ash	Site 4A1	354	0.704324	0.000007
US_A	Lava	Site 66B	3	0.705031	0.000009
Bedded Pumice	Pumice	Site 40C1	3	0.704487	0.000026
Biftu PDC	Ash	Site 9D	17	0.705184	0.000002
WKYP	Pumice	Site 34B	3	0.705184	0.000018
Urji Lava	Lava	Site 37	3	0.704474	0.000013
CO6	Lava	Site 58A	3	0.704507	0.000005

1. See Colby et al., (2022) for information on units and sample locations.
2. 2SD = Two standard deviations

3.2 $^{40}Ar/^{39}Ar$ Dating Results

Further to this new geochemical data we have also dated two units using single crystal $^{40}Ar/^{39}Ar$ dating. We selected the pre-caldera rhyolite lava (SCW_A2; Figure 3) and the welded ignimbrite (NCW_F; Figure 3) which is one of the endmembers for this study. $^{40}Ar/^{39}Ar$ dating

results are presented as probability diagrams in the supplementary information. Weighted mean age uncertainties are reported at 2s hereafter, including J uncertainty, and were calculated using Isoplot 4.0 (Ludwig, 2012). *SCW_A2:* Excluding crystals that gave older ages (see Supplementary Figure B1) single crystal ages are well clustered between 205 to 208 ka. The probability diagram excluding the older crystals displays a main population of crystals (12/15) allowing the calculation of a weighted mean age of 206.7 ± 0.9 ka (MSWD = 0.40, p = 0.95). We interpret this age as the eruption date for this sample. *NCW_F:* The probability diagram is simple showing one single population of crystals (Supplementary Figure B1) allowing calculation of a straightforward weighted mean age of 160.0 ± 0.8 ka (MSWD = 1.03, p = 0.42) that is interpreted as the age of the ignimbrite eruption.

3.3 Mineralogy

The peralkaline rhyolite products at Corbetti are crystal-poor, with only a few samples containing phenocrysts. Here we outline the mineral assemblage of crystal-bearing samples in Table 2 and highlight features of the mineral populations. Details on specific phases present in the basaltic (NCW_H) and peralkaline endmember (welded ignimbrite; NCW_E) focused on in this study are outlined below.

Table 2: Overview of minerals present in crystalline samples from Corbetti Caldera. Mineral abbreviations after Whitney and Evans (2010). Ol: Olivine, Pl: Plagioclase, Aeg: Aegirine Augite, Afs: Alkali-feldspar, Fa: Fayalite, Qz: Quartz, Cpx: Clinopyroxene.

Sample	Material	Groundmass	Minerals	Notes
NCW_H	Basaltic Tuff	Glass shards	Ol, Pl, Fe-Ti Oxides	Aeg and Afs also found in disequilibrium with glass
NCW_F	Welded Ignimbrite	Welded Glass	Qz, Afs, Aeg	Enclave present containing Pl, Afs, Cpx, Fe-Ti oxides
NCW_E	Ignimbrite	Glass	Qz, Afs, rare Aeg and Fa	Qz phenocrysts highly fractured
SCW_B	Lithics from Breccia	Flow-banded glass	Qz, Afs,	Glomerocrysts of Qz and Afs
SCW_D	Lithics from Breccia	Glass	Qz, Afs, Aeg	Glomerocrysts of Qz, rare Afs with granophyric texture. Lithic fragments from other rocks also present

SCW_A2	Lava	Devitrified glass	Qz, Afs, rare Aeg	Qz phenocrysts commonly have embayments. Aeg shows signs of breakdown and resorption
NCW_A	Lava	Devitrified glass	Sparse Aeg	Matrix glass has spherulite texture
Older Obsidians	Obsidian Lava	Glass, Afs microlites	Qz, Afs, Fe-Ti Oxides, rare aegirine-augite	Microlites aligned in flow direction

Olivine

The Basaltic Tuff (NCW_H) contains olivine as individual phenocrysts encased in glass (Figure 9A-D). Olivines are predominantly euhedral to anhedral with some showing slight signs of disequilibrium with patchy zoning (Figure 9D). They range in composition from Fo_{75-85} (Supplementary Figure B2). Olivine's show minor degrees of normal zonation with rare instances of reverse-zoned phenocrysts (Supplementary Figure B2). Some olivine phenocrysts contain Fe-Ti oxide inclusions.

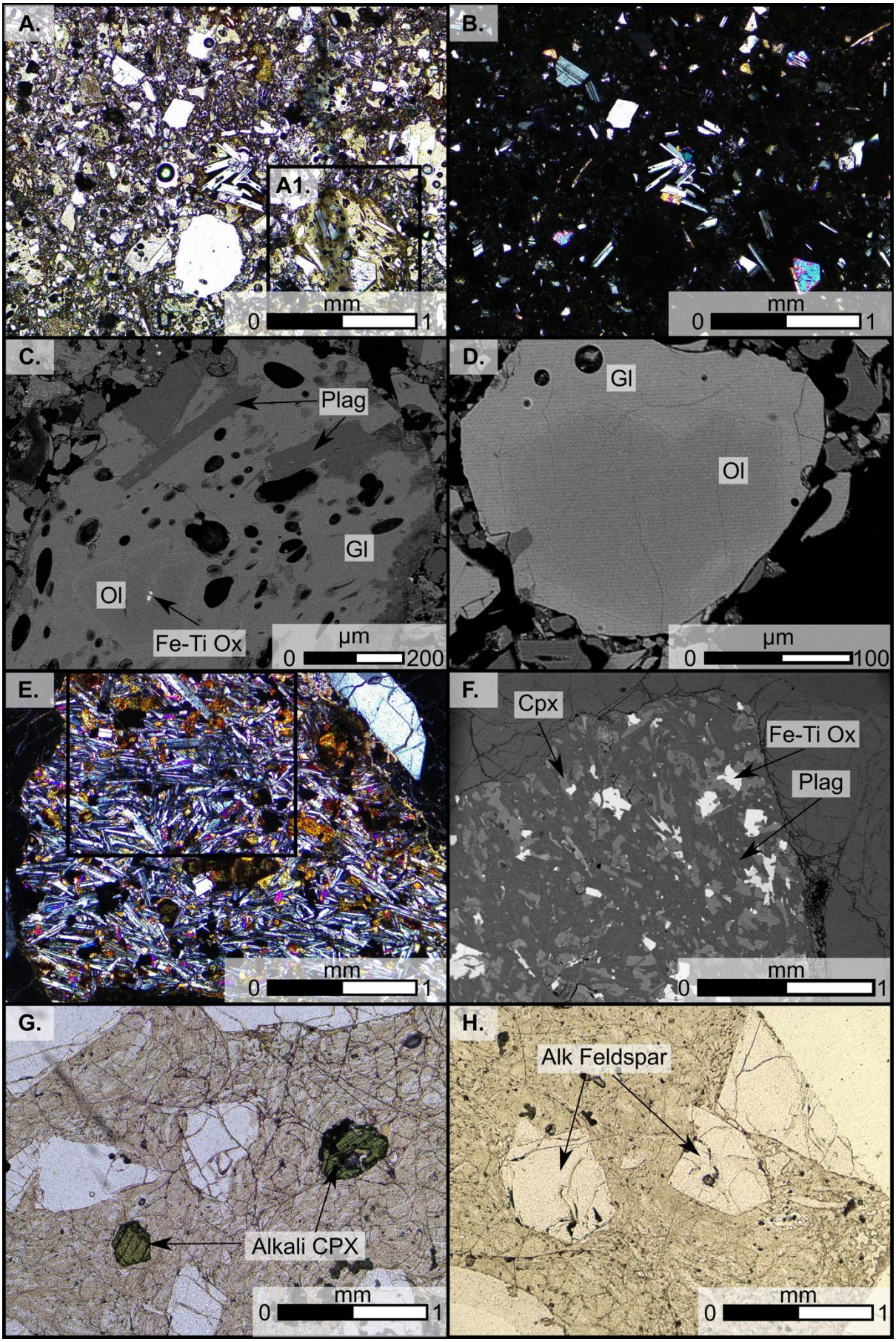
A.
A1.
mm
0
1
B.
mm
0
1
C.
Plag
Gl
Ol
Fe-Ti Ox
µm
0
200
D.
Gl
Ol
µm
0
100
E.
mm
0
1
F.
Cpx
Fe-Ti Ox
Plag
mm
0
1
G.
Alkali CPX
mm
0
1
H.
Alk Feldspar
mm
0
1

Figure 9: A) and B) are thin section images of NCW_H in plane and cross-polarised light. Olivine and plagioclase can be seen hosted in glass. C) shows the area highlighted in A1 in BSE (view of area is rotated ~45^{o} clockwise): presence of plagioclase and olivine hosted in a basaltic glass with visible vesicles. The olivine phenocryst contains Fe-Ti oxide inclusions. D) Olivine phenocrysts hosted in glass. E) Cross-polarised image of crystalline enclave found within NCW_F showing dense concentration of feldspars, clinopyroxenes, and Fe-Ti oxides. F) BSE image of area highlighted in E (View rotated ~90^{o} clockwise). G and H) plane polarised images of NCW_F glass and mineral phases.

Feldspars

The Basaltic Tuff (NCW_H) also contains plagioclase phenocrysts (Figure 9). Core compositions range between An_{63-70}. Rim compositions range between An_{60-70}; however, most phenocryst rims have An concentrations around An_{66-67} (Supplementary Figure B2). Plagioclase phenocrysts show a small degree of normal or reverse zonation (Supplementary Figure B2). Rare alkali feldspars (Or_{36-41}) are also recorded (Figure 10).

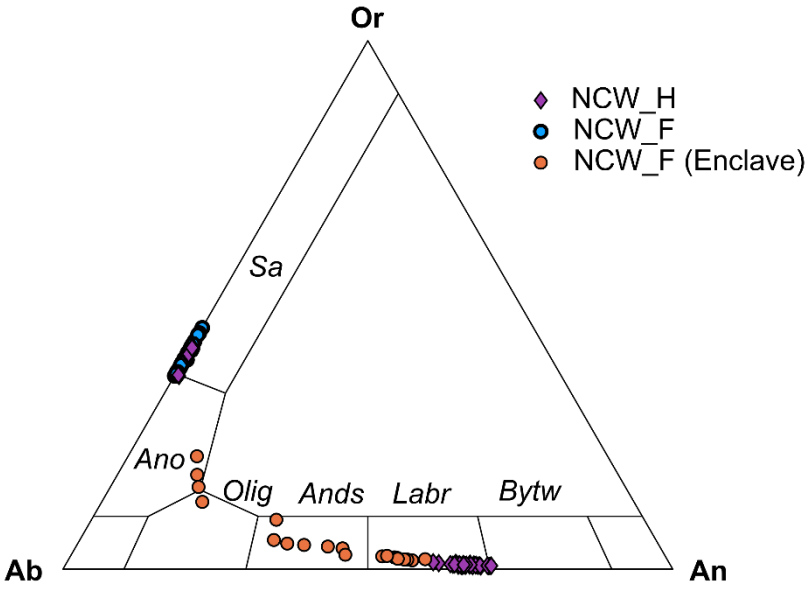

Figure 10: Plot showing the range of feldspar compositions recorded the Basaltic Tuff (NCW_H) and peralkaline ignimbrite (NCW_F) from Corbetti Caldera. The Basaltic Tuff contained several alkali feldspars and the enclave in NCW_F contained a range of plagioclase compositions.

The Welded Ignimbrite (NCW_F) contains abundant alkali feldspars, which range in composition between Or_{36-45}. A crystalline enclave within this sample contains abundant feldspar ranging in composition from An_{11-58} (Figure 9E & 10).

Clinopyroxene

Rare clinopyroxenes are found within the Basaltic Tuff (NCW_H); however, these are not in equilibrium with glass preserved in the sample (established by the equilibrium test employed of Jorgenson et al. (2022), and are likely scavenged from a more evolved melt or accidentally entrained during the eruption.

Clinopyroxenes, whilst scarce, are found within the welded ignimbrite and crystalline enclave and range in composition from Wo_{36} - Wo_{40} and Fs_{39}- Fs_{44}. Alkali clinopyroxenes are also present in large rhyolite flows within the caldera wall (SCW_A1; Colby et al., 2022), however, these show signs of breakdown, likely due to devitrification of the ground-glass or disequilibrium between the cpx and the melt.

Other phases

Quartz is common in all crystalline rhyolitic samples, with phenocrysts in the rhyolitic lavas (SCW_A1) showing embayments. Glomerocrysts of feldspar and quartz are also recorded in the caldera-forming ignimbrite. These are thought to form near the margins of magma systems and are seen in the deposits of other eruptions in the MER (Hutchison et al., 2016b). Fe-Ti oxides are found in a small number of samples as individual grains and inclusions within olivines. A single phenocryst of fayalite was found in NCW_E (ignimbrite associated with the caldera-forming eruption).

4 RhyoliteMELTS Modelling

Thermodynamic modelling of the evolution of Corbetti's magmas was undertaken using RhyoliteMELTS v1.02 (Gualda et al., 2012) using the easyMELTS GUI (Suikkanen, 2020). Isobaric fractional crystallisation of an alkali basalt starting melt was modelled at various pressures (50-250 MPa at 50 MPa intervals), oxygen fugacities (+2 to -2 QFM at 1 log unit intervals) and initial water contents (0.5 and 1-4 wt.% at 1 wt.% intervals). These parameters are consistent with other studies investigating the petrogenesis of peralkaline magmas in the MER (Gleeson et al., 2017; Romano et al., 2020; Scaillet and Macdonald, 2001). The starting composition was chosen to be the most primitive of the glass shards of the Basaltic Tuff, with 6.2 wt.% MgO (Section 3.1). The starting composition for each run was normalised (to 100%) depending on the initial H_2O content and oxygen fugacity (FeOt was recalculated to FeO and

Fe_2O_3 based on the starting fO_2 condition). The modelled compositions of differentiated melts were compared with natural compositions using the least-squared approach of Gleeson *et al.* (2017) to find the best-fit model. RhyoliteMELTS has been used to investigate magma storage conditions at a variety of peralkaline centres (e.g., Peccerillo et al., 2003; Ronga et al., 2009; Gleeson et al., 2017); however, it should be noted that RhyoliteMELTS is not calibrated for peralkaline magmas, previous studies have revealed inaccuracies in its modelling of hydrous phases such as amphibole and apatite (Gualda et al., 2012). Whilst amphibole and apatite are not been reported in Corbetti's eruptive products, they have been found at other MER volcanoes (Gibson, 1974; Peccerillo et al., 2007; Giordano et al., 2014; Tadesse et al., 2023) and in peralkaline melts more generally, and it will likely affect the modelling of intermediate compositions. In addition, RhyoliteMELTS does not accurately model phases such as aenigmatite, commonly found in peralkaline melts (Di Carlo et al., 2010). The crystal-poor nature of Corbetti's erupted products means than many potential phenocryst phases are not seen. These cryptic phases may be present within the crystal mush and have impacted the evolution of these magmas. To overcome some of these limitations, we compare results with petrological data to test the validity of the modelling.

The results from each RhyoliteMELTS simulation are compared with the natural compositions reported in Colby et al. (2022) and Fontijn et al. (2018) using the methodology of Gleeson et al. (2017). This allowed us to determine the best-fit model to the conditions under which Corbetti's magmas evolved (Supplementary Table B1 & Figure 11). Selected pressures from the best fit RhyoliteMELT runs ranged from 100-250 MPa, with most samples evolving at 250 MPa. Best-fit redox conditions for pre-caldera deposits varied at or above (1-2 log units) the QFM buffer; however, the best-fit redox conditions of post-caldera units were found to be at or below the QFM buffer. Initial H_2O concentrations from the best-fit models are consistent at around 0.5 wt.%. There is a considerable variation in the calculated residuals for each target composition, which reflects the deficiencies of RhyoliteMELTS in resolving certain oxide concentrations in these highly peralkaline systems (Fowler and Spera, 2010; Rooney et al., 2012). It may also indicate that the basaltic compositions of the tuff are not reflective of the parental magma source for the peralkaline magmas at Corbetti.

The mineral assemblages predicted by RhyoliteMELTS match reasonably the mineral components observed in natural products going from olivine + plagioclase + clinopyroxene in the basaltic melt to quartz + feldspar + clinopyroxene in the rhyolitic melt. However, the compositions of crystallised clinopyroxenes differ from the observed compositions in natural

samples. In these runs, RhyoliteMELTS does not crystalise alkali-clinopyroxenes which are observed in natural samples (Table 2). This goes some way to explaining the divergence in the predicted liquid lines of descent from the natural data, particularly in the alkali elements. The fractionation of alkali clinopyroxenes would have the effect of lowering the Na_2O concentration in the melt and increasing the proportion of K_2O which would bring the liquid lines of descent in line with the natural data.

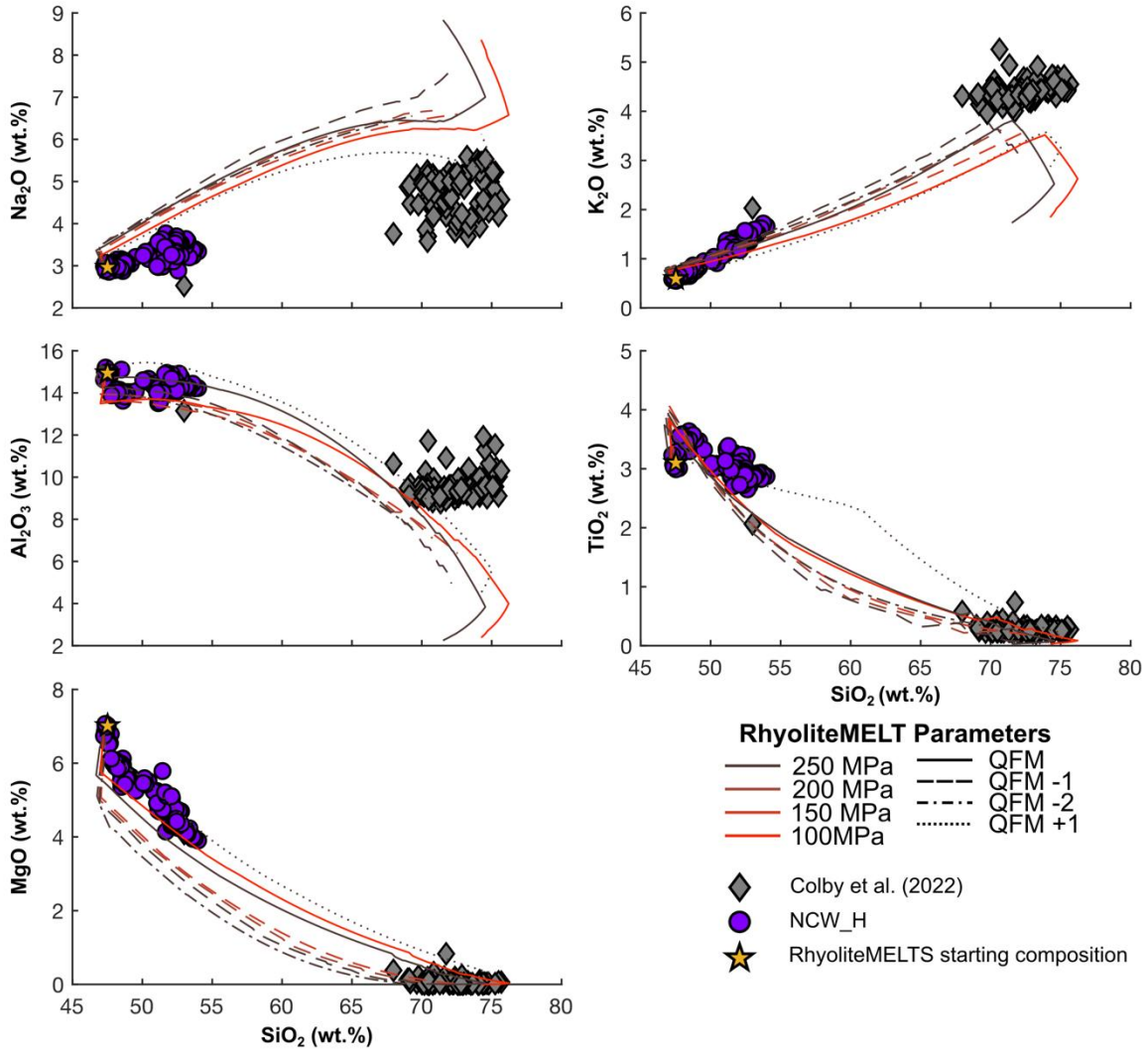

Figure 11: Liquid lines of descent from the best-fit RhyoliteMELTS runs compared to the natural glass (this study) and whole-rock (grey symbols from Colby et al., 2022) data. Star indicates the starting composition used in RhyoliteMELTS. The best fit solutions were determined using the method of Gleeson et al., (2017) to calculate a residual for each run. The residual is calculated through $\sum_X^m(\sum_i^n(X_i - \widehat{X})^2 \ /X_{sd})_X$ *where n is the number of natural samples that represent the target composition, m is the number of oxides considered,* X_i *is the concentration of oxide X of sample i,* $\hat{X}$ *is the concentration of oxide X predicted by*

RhyoliteMELTS at a particular temperature, X_{sd} is the standard deviation of oxide X of all empirically determined compositions of natural samples representing the target composition.

5 Thermometry and Hygrometry

5.1 Basaltic Tuff (NCW_H)

The Basaltic Tuff (NCW_H) was emplaced as a PDC (Colby et al., 2022); therefore, it is likely that a portion of minerals in the sample may not be juvenile and may not be in equilibrium with the erupted glass; hence, only olivine and plagioclase phenocrysts hosted in fresh glass were considered for analysis. All thermometry and hygrometry calculations were conducted using the Thermobar python package (Wieser et al., 2021). For olivine-liquid pairs, the proportion of Fe_2O_3 in the liquid was determined using the method of Kress and Carmichael (1991) at the QFM buffer, which is in line with the results from the thermodynamic modelling (see Section 4) and previous studies (Gleeson et al., 2017). The core and rim compositions of olivine-liquid pairs were tested for equilibrium with their host glass using the method of Roeder and Emslie (1970) (threshold set at $Kd^{Ol-Liq}_{(Fe-Mg)} 0.3 \pm 0.03$; Figure 12), however, other equilibrium tests which are included in the Thermobar package were in good agreement. Equilibrium olivine-liquid pairs were used to estimate temperatures using Equation 22 of Putirka (2008). Temperatures were calculated at five pressures (50 – 250 MPa at 50 MPa intervals) to reflect the proposed depths of magma storage within the MER (Gleeson et al., 2017) and in line with the results of the thermodynamic modelling (see Section 4).

Plagioclase-liquid thermometry and hygrometry calculations were conducted using plagioclase phenocrysts hosted in glass. Temperatures and H_2O contents were calculated iteratively (using 30 iterations) across the same pressure intervals (50-250 MPa at 50 MPa steps) using Equation 24a of Putirka (2008) to calculate temperature and the method of Waters and Lange (2015) to calculate H_2O contents. Results were filtered to exclude plagioclase phenocrysts, which were not in equilibrium with their host glass, using the An-Ab test of Putirka (2008).

Calculated temperatures from olivine-liquid and plagioclase-liquid thermometry range from ~1200 to 1100 °C (Figure 13). Whilst pressure impacts the calculated temperature, the variation is within the error of the models. Due to the low number of equilibrium mineral-liquid pairs,

liquid-only thermometry was also conducted using the Equation 14 of Putirka (2008), which returned gradually decreasing temperatures from ~1200 to 1100 °C across the range in SiO_2 content (Figure 13). These results agree with the olivine-liquid and plagioclase estimates and indicate that equation 14 of Putirka (2008) can be readily applied to alkali basalts where suitable equilibrium mineral-liquid pairs are unavailable. Plagioclase-liquid pairs have a tendency to return slightly higher temperatures than olivine-liquid pairs and glass-only thermometry, however, the data overlap within the thermometry error and are in good agreement with other estimates of alkali basalts from the MER (Tadesse et al., 2023).

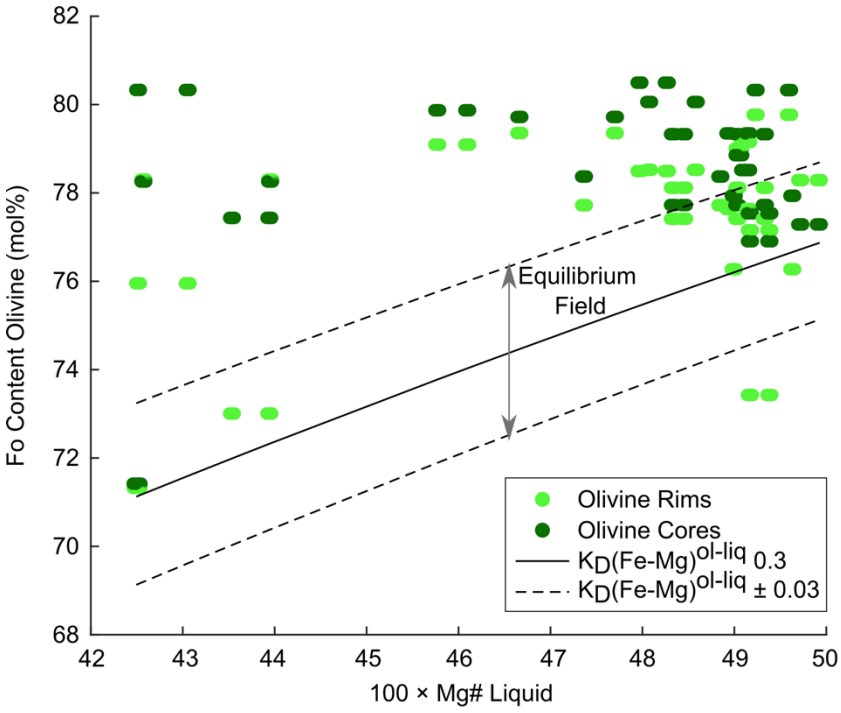

Figure 12: Equilibrium plot showing Fo contents of the rims and cores of olivines plotted against the Mg# of the host glass using the approach of Roeder and Emslie, (1970). Any olivines which plot within the equilibrium field are in equilibrium with the host glass and were used for thermometry (Section 5.1)

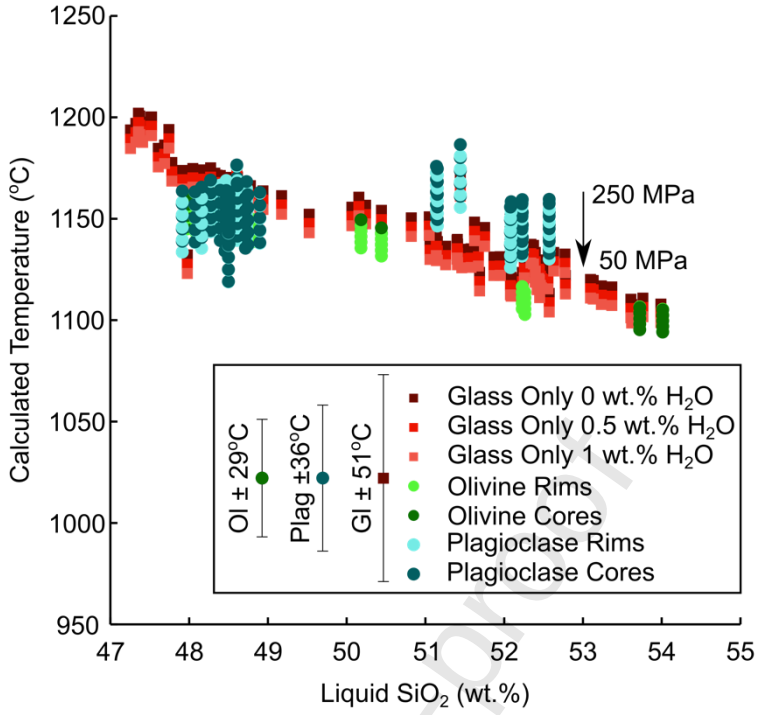

Figure 13: Temperatures calculated using glass-only thermometry, olivine-liquid pairs, and plagioclase-liquid pairs. Glass-only thermometry was calculated assuming three different H_2O contents 0, 0.5 and 1 wt.% H_2O. Olivine and plagioclase temperatures were determined at a range of pressures (250 MPa to 50 MPa at 50 MPa steps). Olivine-liquid temperatures were calculated using Equation 22 of Putirka (2008), and plagioclase-liquid temperatures were calculated using Equation 24a Putirka (2008). Glass-only temperatures calculated with Equation 14 of Putirka (2008).

Due to the lack of crystalline phases, and therefore melt inclusions, in Corbetti's eruptive products, there is minimal information on the pre-eruptive H_2O contents of Corbetti's magmas (Iddon and Edmonds, 2020). We have sought to add to this limited dataset through mineral-liquid hygrometry. Based on equilibrium plagioclase-liquid pairs, we calculated water contents of 0-1.2 ± 0.72 wt.% for Corbetti's basaltic magma. The most anorthic plagioclase returns H_2O contents of ~ 0.2-0.5 wt.%, depending on the pressure used in the calculations. These calculated water contents match well with the estimated initial water contents for the basaltic magma from the RhyoliteMELTS modelling (~ 0.5 – 1 wt.% H_2O; Section 4).

5.2 Peralkaline Rhyolite Ignimbrite (NCW_F)

Temperatures and water contents were also calculated for the peralkaline welded ignimbrite (NCW_F), which outcrops below the Basaltic Tuff (Colby et al., 2022) in Corbetti's northern

caldera wall (Figure 3). Liquid compositions were matched with every feldspar composition and temperatures calculated using Equation 24b of Putirka (2008) in Thermobar (Wieser et al., 2021) across the same pressure intervals (50-250 MPa). Calculated temperatures for equilibrium alkali feldspar-liquid pairs for NCW_F range from 793 to 614 °C (Figure 14). Temperatures below 620 °C were excluded as these are anticipated to be below the solidus (Scaillet and Macdonald, 2001). The variation in pressure had a minimal effect on the calculated temperatures, which is smaller than the model error (±23 °C). Therefore, we have only presented temperatures calculated at 100 MPa for simplicity.

These calculated temperatures were used to estimate water contents using the K-feldspar – liquid hygrometer of Mollo et al. (2015). This hygrometer is calibrated for alkaline melt compositions, which makes it suitable for our samples. The results were filtered using the equilibrium test proposed by Mollo et al. (2015) based on the measured vs predicted Or-Ab partitioning between the K-feldspar and the melt (when $^{Ksp\text{-}melt}Kd_{Or\text{-}Ab}$ 'Measured' versus 'Predicted' is plotted, the equilibrium field lies along the 1:1 line ± 0.05). There is a large range in predicted water concentrations ranging from ~1 wt.% up to 8 wt.% due to the hygrometer's sensitivity to the feldspar's CaO concentration. Slight increases in An result in higher predicted H_2O concentrations. Therefore, we take an average of this data, which returns an H_2O concentration of 5.5 ± 1.2 wt.% (std deviation). This average is only slightly higher than that predicted by RhyoliteMELTS. To test if the calculated water content is a reasonable estimate, we calculated the solubility of H_2O in the melt as a function of composition, temperature and pressure using the method of Allabar et al. (2022). These results demonstrate up to ~7.5 wt.% H_2O can be dissolved in a peralkaline melt at 250 MPa.

Temperatures were also estimated for a crystalline enclave found within NCW_F. As no glass compositions could be collected, we used two-feldspar thermometry (equation 27b of Putirka, 2008), and the clinopyroxene-only thermobarometry using the random forest model developed by Jorgenson et al. (2022). We employed the equilibrium model of Elkins and Grove (1990) for the two-feldspar thermometry (see supplementary information for details). Plagioclase phenocrysts were only in equilibrium with three alkali feldspar phenocrysts. Calculated temperatures ranged from 879 to 711.9 ± 30 °C, varying by ~ 12 °C across the pressure range for a given pair. This is consistent with expected temperatures for less evolved melt where a two-feldspar phases are present.

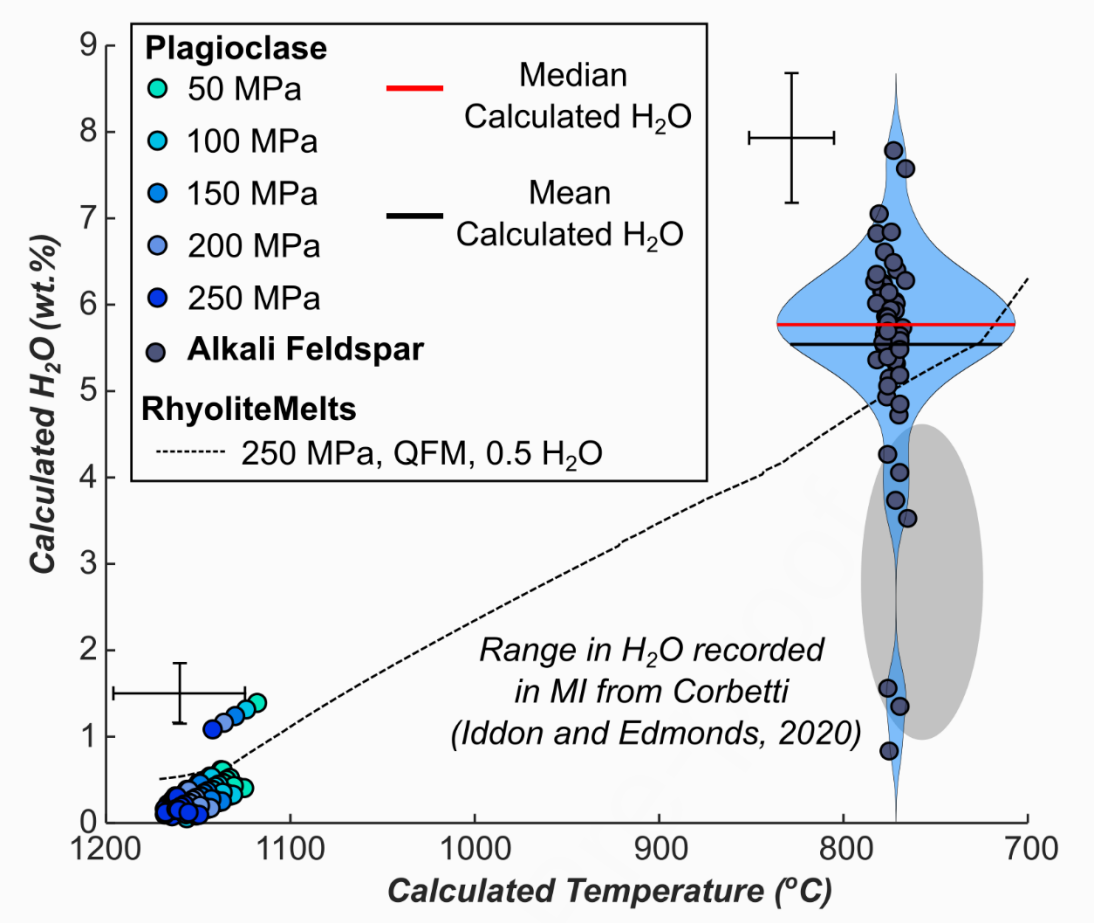

Figure 14: Calculated temperatures and water contents of plagioclase-liquid pairs and alkali feldspar-liquid pairs. Plagioclase-liquid pairs were calculated across a range of pressures to reflect the range of values used for the RhyoliteMELTS modelling. Alkali-feldspar pairs are overlain by a kernel density violin plot (blue region) showing the distribution of the data and the mean and median values. Data overlain with RhyoliteMELTS output, which best matches the natural composition of the welded ignimbrite. Grey region shows the range in H_2O contents found in melt inclusions from Corbetti (Iddon and Edmonds, 2020). Plagioclase-liquid temperatures and H_2O contents were calculated using Equation 24a of Putirka (2008) and Waters and Lange (2015), respectively. Kspar-liquid temperatures and H_2O contents were calculated using Equation 24b of Putirka (2008) and Mollo et al. (2015), respectively. Error bars reflect the model error (Section 5).

5.3 Barometry

Reliable pressure estimates based on clinopyroxene-liquid barometry depend on the availability of equilibrium clinopyroxene-liquid pairs. Clinopyroxene phenocrysts from the welded ignimbrite (NCW_F) were not in equilibrium with their host liquids following the equilibrium test employed by Jorgenson et al. (2022). In addition, they had an abundance of Fe cations and a deficiency in Al cations and were not considered for the barometry.

Clinopyroxenes in the crystalline enclave found in NCW_F did have the correct cation site occupancies and good analytical totals however, no liquid compositions from the enclave could be analysed. Therefore, we conducted clinopyroxene-only barometry using Jorgenson et al.'s (2022) random forest machine learning algorithm. Analysed clinopyroxenes returned average mean temperatures of 1081 ºC (standard deviation = 15 ºC, calibration error = 72.2 ºC) and average pressures of 110 MPa (standard deviation = 30 MPa, calibration error = 320 MPa, range 70 – 190 MPa). The large error associated with the pressure estimates results from the calibration set used in the model (Jorgenson et al., 2022) and uncertainties associated with clinopyroxene-only thermobarometers. Tadesse et al. (2023) note that the clinopyroxene-only thermometer of Jorgenson et al. (2022) overestimates temperatures in peralkaline systems compared with other thermometers; however, it gives good agreement with other estimates of pressure. Further experimental work on alkali clinopyroxenes is necessary to expand the training dataset and refine the errors on this model.

6 Discussion

6.1 New constraints on eruptive history

The new dating of two units from Corbetti has yielded high-precision dates, allowing further refinement of the timescales of eruptive activity within the complex. A pre-caldera lava flow (SCW_A2) is dated to 206 ky, and the inferred post-caldera ignimbrite and focus of this study, NCW_F, is dated to 160 ky. These timings bracket the ca. 182 ka caldera-forming eruption in accordance with the mapped field stratigraphy and provide further validation for this date. These new dates agree well with the relative stratigraphy outlined in Colby et al. (2022) and highlight the pre-caldera shield was built up over the course of at least 30 ky prior to the caldera-forming eruption ~182 ka (Hutchison et al., 2016a; Vidal et al., 2022b). There was then likely a period of relative quiescence following the caldera-forming eruption before the eruption of the welded ignimbrite (NCW_F). The length of this quiescence is difficult to establish as smaller eruptions may have occurred that have not been captured in the stratigraphy.

6.2 The Basaltic Eruption

The Basaltic Tuff (NCW_H) is the only basaltic eruption product recorded within Corbetti Caldera. The eruption was phreatomagmatic, likely interacting with groundwater or a pre-existing intra-caldera lake (Colby et al., 2022). The weakly peralkaline obsidian chips found within the sample have a very similar composition to the obsidian flows found outside the caldera wall (Older Obsidians of Colby et al. (2022); Figure 5). This suggests the magma likely erupted through an obsidian dome/flow that had been emplaced during the pre-caldera phase of activity. Glass shard compositions vary from basaltic to basaltic-andesite, with limited variation in composition within individual shards. Figure 6 highlights some scatter in certain major elements (as outlined in Section 3.1), which may reflect magma stored in distinct melt lenses with slightly heterogeneous compositions. It is well documented that peralkaline magmas predominantly evolve through fractional crystallisation (Dambly et al., 2024; Gleeson et al., 2017; Hutchison et al., 2018; White et al., 2023) and the compositions recorded in the Basaltic Tuff reflect a fractional crystallisation trend (Figure 6) as demonstrated by the RhyoliteMELTS modelling with the trends in the data following similar trends to the predicted liquid lines of descent. Variations from these trends are mainly due to the RhyoliteMELTS not fractionating alkali pyroxene phases, as outlined in Section 4. The fractional crystallisation trend suggests the eruption tapped a compositionally zoned magma system. Figure 5 shows an overview of basaltic compositions from a selection of the calderas within the MER. Compared to other MER calderas (Figure 5), Corbetti shows slightly lower alkali contents than the general trend of the rift. These lower alkali contents may explain the observed discrepancy between modelled Na_2O and K_2O concentrations from RhyoliteMELTS and natural samples (Figure 14). This discrepancy was not observed by Gleeson et al. (2017) and, therefore, may indicate that this basaltic unit does not accurately reflect the parental basalt from which the peralkaline products are derived. In the absence of other basaltic eruptions recorded at Corbetti, this is difficult to test; however, the lower concentration of alkali elements in this unit compared with other basalts from the MER may support this hypothesis. Further field investigation would be necessary to attempt to identify additional basaltic eruptions within the caldera to explore this hypothesis further.

Most olivine phenocrysts show no or very slight normal zonation (Figure 9 and Supplementary Figure B2). This is consistent with them being formed within a fractionally crystallising liquid. Sparse reverse-zoned phenocrysts indicate some transfer or scavenging of olivines into a more primitive melt region. As these phenocrysts have not started to re-equilibrate with the host glass

it suggests they were incorporated immediately before eruption and quenching. Similarly, plagioclase phenocrysts show both normal and reverse zoning (Supplementary Figure B2), again suggesting some scavenging or transfer of phenocrysts. In addition to this, the presence of alkali feldspars and alkali clinopyroxenes suggests scavenging or entrainment of felsic phases into the melt, potentially from a crystalline mush, before the eruption.

Temperatures determined from olivine-liquid pairs, plagioclase-liquid pairs and glass-only thermometry, show a gradual decrease in melt temperature from 1200 °C to ~1100 °C, consistent with a cooling and fractional crystallisation trend. These estimates also agree with olivine crystallisation temperatures in the MER (Wong et al., 2022).

The water contents determined for Corbetti's basaltic magma (0 – 1.2 wt.% H_2O) add to the sparse dataset on H_2O contents in basaltic magmas from volcanoes in the MER. These data are consistent with estimates from olivine-hosted melt inclusions from Kone and Butajira (0.2 – 1.5 wt.%) (Iddon and Edmonds, 2020) and with H_2O contents in transitional basaltic melts and alkali basalts from Pantelleria, Italy (White et al., 2009; Gioncada and Landi, 2010; Neave et al., 2012; Gleeson et al., 2017). This hygrometry also supports the best-fit models from the RhyoliteMELTS modelling (Section 4, Table 2), which indicated an initial H_2O content of 0.5-1 wt.% and is consistent with the results of RhyoliteMELTS modelling on other silicic systems in the MER (Gleeson et al., 2017). This demonstrates that whilst RhyoliteMELTS has limitations when investigating peralkaline melts (Gleeson et al., 2017; Romano et al., 2020), it does offer a good approximation of the initial starting H_2O composition. This finding helps to support previous studies which have exclusively used RhyoliteMELTS to infer the initial water content of alkali basaltic magmas (Gleeson et al., 2017).

In summary, our findings indicate basaltic pre-eruptive temperatures at Corbetti are consistent with other estimates for the MER and peralkaline systems elsewhere. Evidence from olivine and plagioclase phenocrysts and the presence of more felsic phases (alkali clinopyroxenes and alkali feldspars) indicate some degree of scavenging of phenocrysts prior to eruption. Our estimate of the H_2O content of the alkali basalt of around 0.5 wt.%, is consistent with estimates from olivine-hosted melt inclusions, and with RhyoliteMELTS modelling presented in this study and previous studies on calderas in the MER (Gleeson et al., 2017).

6.3 Peralkaline Magmas

Our RhyoliteMELTS observations support those of previous studies, indicating that ~90% fractional crystallisation is needed to reach peralkaline compositions (Gleeson et al., 2017).

Incompatible trace element plots highlight the role of fractional crystallisation in the evolution of Corbetti's magmas (Figure 7), and the characteristic depletion in Ba and Sr observed (Figure 8) highlights the removal of alkali feldspars, a key component of peralkaline melts (Carmichael and MacKenzie, 1963; Macdonald et al., 2021; White et al., 2023). However, Figure 7 shows a considerable scatter in the concentration of Nb, with some samples showing elevated Zr/Nb ratios of up to 20. High Zr/Nb values have been attributed to the crystallisation of ilmenite (Hutchison et al., 2018); however, these high Zr/Nb ratios may indicate a differing source composition when viewed alongside the high Zr/Hf ratios. This may indicate some heterogeneity in source compositions at Corbetti, where basaltic magmas have variable initial Nb, Hf and Ta concentrations and have followed different liquid lines of descent to reach a near-homogenous compositional endpoint.

The trace element data (Figure 7) indicates that fractional crystallisation was the dominant evolutionary mechanism, with crustal assimilation unlikely to play a major role. This is supported by Sr isotope analysis (Supplementary Table B1) on samples that span the main pre- and post-caldera eruptions, which shows no evidence that crustal assimilation occurred during these magmas' evolution (Figure 16). One exception is the ignimbrite associated with the caldera-forming eruption (NCW_E), which shows an elevated ($^{87}Sr/^{86}Sr$ ~ 0.706) signature, consistent with some contamination by country rock during magma evolution. This was also observed by Rapprich et al. (2016), who proposed the elevated ratio resulted from 0.5 % contamination by an Ethiopian basement component ($^{87}Sr/^{86}Sr$ ~ 0.731; Peccerillo et al., 1998). All other samples show limited variation in isotopic ratios ($^{87}Sr/^{86}Sr$ from 0.704 to 0.705); these values fall within the MER's observed range and align with previous data (Figure 15). Whole rock analysis of $^{87}Sr/^{86}Sr$ ratios in Sr-poor peralkaline rhyolites can return heterogeneous results for a single sample even in fresh aphyric samples (Deniel, 2009). Deniel (2009) proposed that small changes in $^{87}Sr/^{86}Sr$ ratios may reflect interaction with magmatic fluids prior to eruption as opposed to a crustal signature. Further investigation with additional isotopic analysis is required to evaluate this hypothesis at Corbetti.

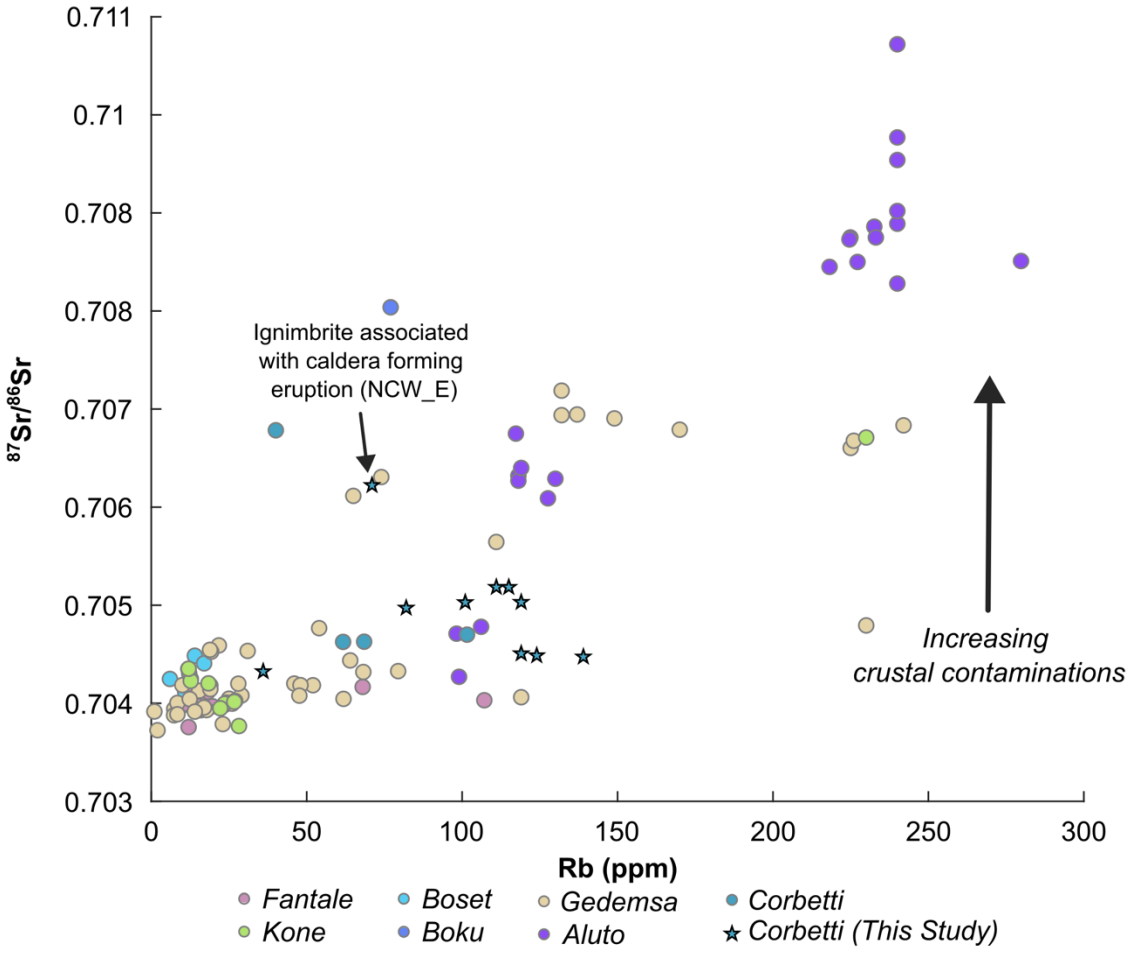

Figure 16: Variation in $^{87}Sr/^{86}Sr$ ratio values reported across the MER in comparison to the values in this study. One of Corbetti's eruptive units (NCW_E) records an elevated $^{87}Sr/^{86}Sr$ ratio indicating a degree of crustal contamination that may result from the incorporation of country rock during eruption or through assimilation of country rock due to a higher magma flux in the development of this magma body. Other samples from Corbetti show similar values with some slight elevations observed which may indicate a minor degree of crustal contamination but are in line with other samples from the MER. Data downloaded from the GeoRoc database (downloaded on 1st Dec 2023 https://georoc.eu/). Fantale: Furman et al. (2006); Giordano et al. (2014); Ayalew et al. (2016); Kone: Furman et al. (2006); Peccerillo et al. (2007); Ayalew et al. (2016); Boset: Furman et al. (2006); Ronga et al. (2009); Ayalew et al. (2016); Boku: Boccaletti et al. (1995); Gedemsa: Boccaletti et al. (1995); Barberio et al. (1999); Peccerillo et al. (2003); Giordano et al. (2014); Ayalew et al. (2016); Castillo et al. (2020); Aluto: Deniel (2009); Corbetti: Rapprich et al. (2016)

As our understanding of the evolutionary conditions required to generate peralkaline magmas has increased, it is clear that the extreme compositions of these magmas can be attained under a range of storage conditions. Geophysical and petrological investigations in the MER highlight zones at multiple depths in the crust where peralkaline magmas can be stored and evolve by cooling and crystallisation towards highly-differentiated compositions (Gleeson et al., 2017; Iddon and Edmonds, 2020; Samrock et al., 2021). This process has been explained in calc-alkaline systems through the role of reactive flows where a melt in a low melt fraction mush is buffered by the surrounding crystalline phases (Blundy, 2022; Dufek and Bachmann, 2010). As the melt evolves it is extracted from the system via buoyant rise, or compaction. Peralkaline rhyolites typically have a lower viscosity compared to calc-alkaline rhyolities (Di Genova et al., 2013; Hughes et al., 2017) and therefore, this process of melt-crystal separation could explain the scarcity of minerals in most of Corbetti's products. It would also explain the petrological evidence for the scavenging of alkali feldspars from melts at different stages of differentiation (Iddon et al., 2019), whereby extracted melt interacts with regions of more evolved crystalline mush prior to eruption entraining more evolved phases. Further phase equilibrium experiments are required on peralkaline melts at various pressure and temperature conditions, coupled with model simulations, to develop and evaluate the hypothesis that crystal-free peralkaline magmas can be readily extracted from mush-rich crustal reservoirs.

Feldspar-liquid hygrometry returns a range of water contents from 1 to ~8 wt.% H_2O. This is due to the sensitivity of the hygrometer to the CaO content of the feldspar. Taking an average of these data (Figure 14) suggests that the peralkaline magmas at Corbetti had a pre-eruptive water content of ~ 5.5 ±1.2 wt.% (Std deviation) wt.% H_2O (Figure 14). This is higher than previous estimates of water contents at Corbetti obtained from melt inclusions, which suggested H_2O contents of 0.95-4.2 wt.% and CO_2 concentrations of < 330 ppm (Iddon and Edmonds, 2020). In addition, our calculated water contents match those of other peralkaline systems in the MER, with melt inclusions from Aluto recording a maximum of 8 wt.% H_2O, demonstrating the hydrous nature of these magmas (Iddon and Edmonds, 2020). Estimated k-feldspar-liquid temperatures (~793 °C) align well with expected pre-eruptive temperatures for peralkaline magmas at other centres in the MER (Gleeson et al., 2017; Tadesse et al., 2023).

The rarity of melt inclusions in Corbetti's eruptive products makes it challenging to understand the magma storage system, particularly when no primitive or intermediate melt inclusions are recorded. Alkali-feldspar hygrometry provides evidence for the hydrous nature of these melts. In the case of Corbetti, high-water contents may be the main driving force behind explosive

volcanic eruptions, as the shallow storage region would likely result in the majority of CO_2 being degassed well before an eruption.

6.4 Depth of magma storage

Constraining the magma storage depths at Corbetti through petrological analysis is challenging due to the lack of suitable crystal phases and the significant uncertainties associated with single-phase thermobarometry. As outlined in section 5.3, clinopyroxene-only barometry returns a mean pressure of ~110 MPa (standard deviation of 30 MPa, calibration error 320 MPa) which corresponds to storage depths of 2.3 - 6.9 km using a crustal density of 2800 gm^{-3} (Wilks et al., 2017). These estimates are similar to clinopyroxene-only barometry calculations at Bora Baricha - Tullu Moye with estimated storage depths of < 200 MPa (Tadesse et al., 2023). The large uncertainties on this estimation results from the limited experimental P, T, XH_2O dataset in the machine-learning calibration for clinopyroxenes in peralkaline melts. Further experimental work will help to improve the calibration and reduce uncertainties in the model. Similarly, our findings from RhyoliteMELTS modelling (Section 4), suggest magma at Corbetti has been stored at pressures ranging from 100-250 MPa, with most magma likely stored at depths greater than 200 MPa (Supplementary Table B1). This corresponds to depths of ca. 4 – 9 km (density of 2800 gm^{-3} Wilks et al., 2017). This overlaps with estimates previously determined for other peralkaline systems in the rift using RhyoliteMELTS (e.g., ~150 MPa at Aluto; Gleeson et al., 2017), and for Aluto (50-300 MPa) determined from quartz-hosted melt inclusions (Iddon and Edmonds, 2020), reinforcing the view that shallow storage pressures are necessary for the generation of peralkaline melts within the MER.

Comparing our findings with geophysical observations from Corbetti shows a good alignment between the various techniques (Figure 14). Magnetotelluric data have also shown the presence of a hot conductive layer around 5-15 km depth (Gíslason *et al.*, 2015; Wilks *et al.*, 2017; Lloyd *et al.*, 2018) interpreted as a region of partial melt (Gíslason et al., 2015). Numerical modelling of the causes of the observed uplift at Corbetti (Lloyd et al., 2018) concluded that the injection of mafic magma at ~7 km depth could explain the observed deformation (Gottsmann et al., 2020; Albino and Biggs, 2021). Dambly et al., (2024) used magnetotelluric data to infer the presence of a shallow magmatic mush ~ 4 km depth with between 20-35 vol% melt, fed by a basaltic magma source with around 6-16 vol% melt at > 16 km depth (Figure 15).

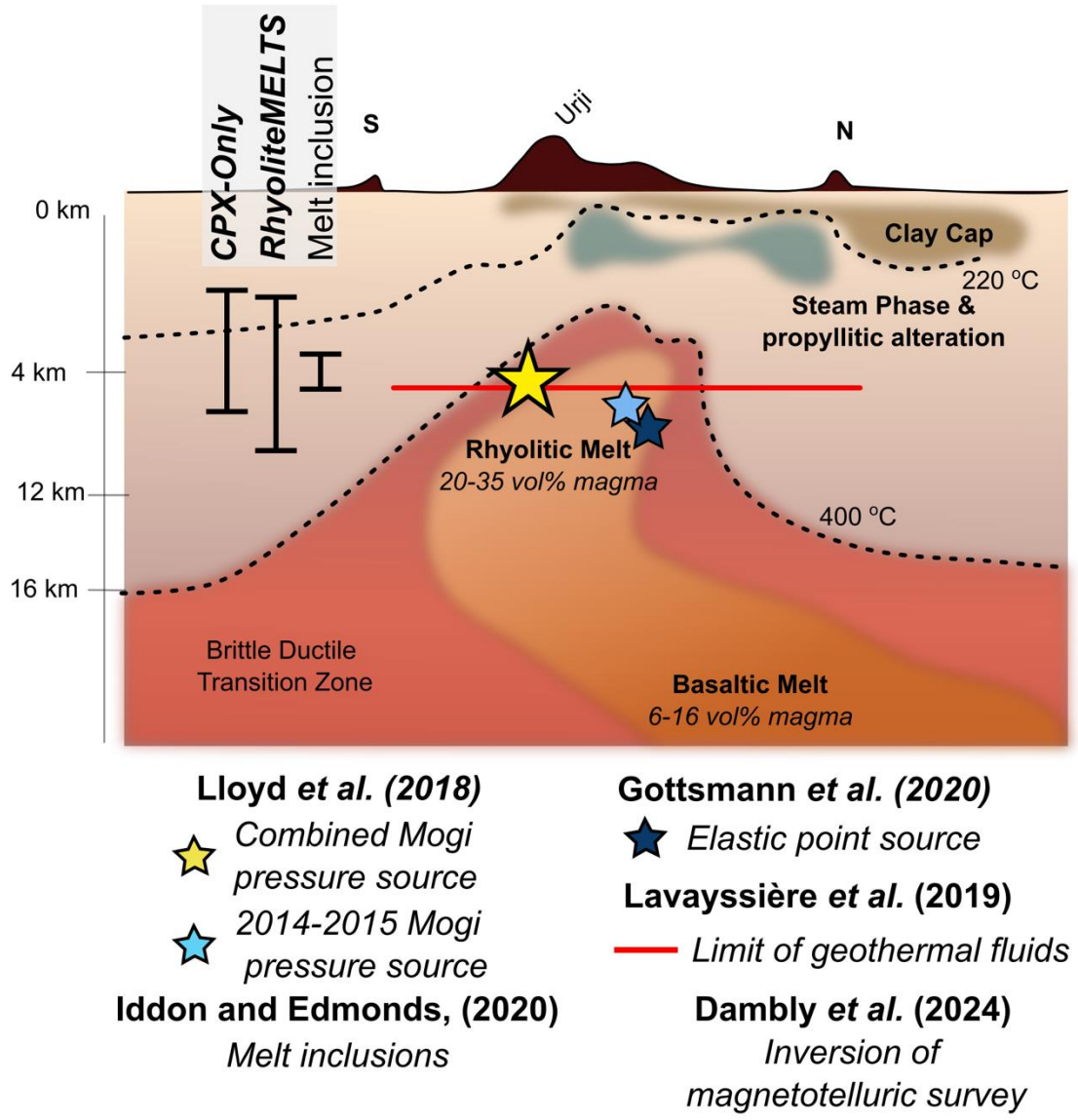

Figure 15: Schematic diagram adapted from Dambly et al. (2024) showing the proposed structure of Corbetti's magmatic system from magnetotelluric data. The location of the proposed sources of inflation (Mogi) from Lloyd et al. (2018) and Gottsmann et al. (2020) are overlain for comparison. The depth ranges from melt inclusion data, CPX-barometry (this study) and RhyoliteMELTS modelling (this study) are also shown for comparison and show good agreement with the geophysical data. A table summarising these data can be found in the supplementary information, Table B2.

Whilst the data on magma storage depths at Corbetti are limited and uncertain, we show the results from this study align well with other independent petrological and geophysical observations that all demonstrate the importance of low pressures in the evolution of peralkaline systems. Nonetheless, there is considerable need for further experimental studies

particularly encompassing higher pressures, temperatures and volatile-rich compositions, focussing specifically on peralkaline products from the MER to gain a better understanding of the phase relationships and storage conditions throughout the crust beneath silicic volcanoes in the MER.

7 Conclusions

New age data has further constrained the timescales of volcanism at Corbetti, demonstrating that shield-building activity, through the eruption of large rhyolitic lava flows, occurred at least 30 ky prior to the caldera-forming eruption (182 ka; Hutchison et al., 2016; Vidal et al., 2022). The dating of a post-caldera ignimbrite to 160 ka adds an additional constraint on the age of caldera formation and highlights a potential period of quiescence after the caldera-forming eruption. These dates provide more details about the timings from pre-caldera to post-caldera activity and support the proposed chronology of Colby et al. (2022). These new dates also contribute to our understanding of timescales for the early evolution of calderas within the MER.

Detailed geochemical analysis of the only recorded basaltic eruption from within Corbetti Caldera and a peralkaline ignimbrite has allowed us to explore the endmember compositions of recorded at Corbetti. The alkali-basaltic magmas erupted at Corbetti were likely tapped from a compositionally zoned magma system evidenced by the range of compositions found within the deposit. RhyoliteMELTS modelling and trace element geochemistry indicate that Corbetti's magmas likely evolved through progressive fractionation, and $^{87}Sr/^{86}Sr$ isotope values rule out anything other than a minor role for crustal assimilation. Additionally, by combining RhyoliteMELTS modelling with thermometry, hygrometry and barometry we show that the alkali-basalt had ~0.2 -1wt.% H_2O and had an estimated temperatures for the basaltic magmas ranged from 1200 °C to 1100 °C, in agreement with other studies in the MER (Wong et al., 2022).

Hygrometry on the peralkaline end member suggests a water content of ~5.5 wt.%. Although higher than previous estimates for Corbetti, it does agree with other data from peralkaline systems in the MER and globally. Although further constraints on the volatile contents of Corbetti's magmas are needed, particularly regarding the halogen contents, this data does highlight the hydrous nature of Corbetti's magmas and demonstrates the important role H_2O plays in the explosive eruption of these magmas.

There are still considerable uncertainties surrounding estimating magma storage depth within peralkaline systems using standard modelling or petrological techniques. Pressure estiamtes presented here suggest storage of peralkaline magmas at < 200 MPa highlighting that shallow storage is a key factor in the generation of peralkaline melts. These findings are in good agreement with independent geophysical observations at Corbetti. Currently, geophysical estimates provide the best insight into magma storage beneath Corbetti, with further experimental work needed to refine the current barometers to apply to these shallow magmatic systems with a particular focus required on the products of the MER.

Overall, the scarcity of crystalline phases at Corbetti hampers efforts to petrologically resolve the magmatic processes governing evolution compared with other silicic centres in the MER. However, this absence of crystalline phases highlights the efficacy of crystal-melt segregation processes in these highly differentiated systems. Further work is required to investigate the mechanisms of melt extraction within peralkaline systems.

8 Acknowledgements

This work was supported by the Natural Environment Research Council via grant NE/L013932/1 (RiftVolc) and an Oxford DTP studentship (NE/L002612/1) to D.C. K.F. acknowledges Fonds National de la Recherche Scientifique (F.R.S.-FNRS) MIS grant F.4515.20. K.F., D.P. and T.M. acknowledge the Wiener Anspach Foundation grant “The Magmatic Evolution of Geothermally Active Calderas in Ethiopia”. We would like to thank Seid Abubaker of Ethioder and guide Hamiyou Bekera for their support in the field and for ensuring a safe and productive field trip. Fieldwork and sample export were kindly permitted by the authorities of the Oromia region and the Ministry of Mines and Petroleum of Ethiopia, respectively. We thank Ed Llewellin for editorial handling of this paper and Margaret Hartley and Shane Rooyakkers for their thorough and constructive reviews which have greatly improved this paper. We would also like to thank Owen Green for his help with sample preparation and microscopy, Matthew Beverley Smith for making the thin sections of selected samples, Andrew Matzen for his help and support in setting up and using the EMPA and Victoria Smith for additional analysis, Activation Laboratories for undertaking the whole rock geochemical analysis, and Wendy Debouge and Jeroen de Jong for Sr isotope analysis.

9 References

Agostini, A., Bonini, M., Corti, G., Sani, F., Mazzarini, F., 2011. Fault architecture in the Main Ethiopian Rift and comparison with experimental models: Implications for rift evolution and Nubia-Somalia kinematics. Earth Planet. Sci. Lett. 301, 479–492. https://doi.org/10.1016/j.epsl.2010.11.024

Albino, F., Biggs, J., 2021. Magmatic Processes in the East African Rift System: Insights From a 2015–2020 Sentinel-1 InSAR Survey. Geochem. Geophys. Geosystems 22, e2020GC009488. https://doi.org/10.1029/2020GC009488

Albino, F., Biggs, J., Lazecký, M., Maghsoudi, Y., 2022. Routine Processing and Automatic Detection of Volcanic Ground Deformation Using Sentinel-1 InSAR Data: Insights from African Volcanoes. Remote Sens. 14, 5703. https://doi.org/10.3390/rs14225703

Allabar, A., Petri, P.L., Eul, D., Nowak, M., 2022. An empirical H_2O solubility model for peralkaline rhyolitic melts. Contrib. Mineral. Petrol. 177, 52. https://doi.org/10.1007/s00410-022-01915-8

Balbas A., Koppers A. A., Kent D. V., Konrad K., Clark P. U. (2016). Identification of the short-lived Santa Rosa geomagnetic excursion in lavas on Floreana Island (Galapagos) by $^{40}Ar/^{39}Ar$ geochronology. *Geology, 44*, 359-362.

Biggs, J., Ayele, A., Fischer, T.P., Fontijn, K., Hutchison, W., Kazimoto, E., Whaler, K., Wright, T.J., 2021. Volcanic activity and hazard in the East African Rift Zone. Nat. Commun. 12, 6881. https://doi.org/10.1038/s41467-021-27166-y

Blundy, J., 2022. Chemical Differentiation by Mineralogical Buffering in Crustal Hot Zones. J. Petrol. 63, egac054. https://doi.org/10.1093/petrology/egac054

Brotzu, P., Morbidelli, L., Piccirillo, E.M., Traversa, G., 1980. Volcanological and magmatological evidence of the Boseti volcanic complex (Main Ethiopian Rift). Acc Naz Lincei Roma 47, 317–362.

Carmichael, I.S.E., MacKenzie, W.S., 1963. Feldspar-liquid equilibria in pantellerites; an experimental study. Am. J. Sci. 261, 382–396. https://doi.org/10.2475/ajs.261.4.382

Chernet, T., Hart, W.K., 1999. Petrology and geochemistry of volcanism in the northern Main Ethiopian Rift-southern Afar transition region. Acta Vulcanol. 11, 21–42.

Colby, D.J., Pyle, D.M., Fontijn, K., Mather, T.A., Melaku, A.A., Mengesha, M.A., Yirgu, G., 2022. Stratigraphy and eruptive history of Corbetti Caldera in the Main Ethiopian Rift. J. Volcanol. Geotherm. Res. 428, 107580. https://doi.org/10.1016/j.jvolgeores.2022.107580

Cox S. E., Hemming S. R., Tootell D. (2020). The Isotopx NGX and ATONA faraday amplifiers. *Geochronology*, *2*, 231-243.

Dambly, M.L.T., Samrock, F., Grayver, A., Eysteinsson, H., Saar, M.O., 2024. Geophysical imaging of the active magmatic intrusion and geothermal reservoir formation beneath the Corbetti prospect, Main Ethiopian Rift. Geophys. J. Int. 236, 1764–1781. https://doi.org/10.1093/gji/ggad493

Di Carlo, I., Rotolo, S.G., Scaillet, B., Buccheri, V., Pichavant, M., 2010. Phase equilibrium constraints on pre-eruptive conditions of recent felsic explosive volcanism at Pantelleria Island, Italy. J. Petrol. 51, 2245–2276. https://doi.org/10.1093/petrology/egq055

Di Genova, D., Romano, C., Hess, K.U., Vona, A., Poe, B.T., Giordano, D., Dingwell, D.B. and Behrens, H., 2013. The rheology of peralkaline rhyolites from Pantelleria Island. *Journal of Volcanology and Geothermal Research*, *249*, pp.201-216.

Dufek, J., Bachmann, O., 2010. Quantum magmatism: Magmatic compositional gaps generated by melt-crystal dynamics. Geology 38, 687–690. https://doi.org/10.1130/G30831.1

Ebinger, C.J., 2005. Continental break-up: The East African perspective. Astron. Geophys. 46, 2.16-2.21. https://doi.org/10.1111/j.1468-4004.2005.46216.x

Elkins, L.T. and Grove, T.L., 1990. Ternary feldspar experiments and thermodynamic models. *American Mineralogist*, *75*(5-6), pp.544-559

Ferla, P., Meli, C., 2006. Evidence of Magma Mixing in the 'Daly Gap' of Alkaline Suites: a Case Study from the Enclaves of Pantelleria (Italy). J. Petrol. 47, 1467–1507. https://doi.org/10.1093/petrology/egl015

Fontijn, K., McNamara, K., Zafu Tadesse, A., Pyle, D.M., Dessalegn, F., Hutchison, W., Mather, T.A., Yirgu, G., 2018. Contrasting styles of post-caldera volcanism along the Main Ethiopian Rift: Implications for contemporary volcanic hazards. J. Volcanol. Geotherm. Res. 356, 90–113. https://doi.org/10.1016/j.jvolgeores.2018.02.001

Fowler, S.J., Spera, F.J., 2010. A metamodel for crustal magmatism: Phase equilibria of giant ignimbrites. J. Petrol. 51, 1783–1830. https://doi.org/10.1093/petrology/egq039

Furman, T., Bryce, J., Rooney, T.O., Hanan, B., Yirgu, G., Ayalew, D., 2006. Heads and Tails: 30 million years of the Afar plume. Afar Volcan. Prov. East Afr. Rift Syst. 259, 95–119.

Gibson, I.L., 1974. A Review of the Geology, Petrology and Geochemistry of the Volcano Fantale. Bull. Volcanol. 791–802.

Gioncada, A., Landi, P., 2010. The pre-eruptive volatile contents of recent basaltic and pantelleritic magmas at Pantelleria (Italy). J. Volcanol. Geotherm. Res. 189, 191–201. https://doi.org/10.1016/j.jvolgeores.2009.11.006

Giordano, F., D'Antonio, M., Civetta, L., Tonarini, S., Orsi, G., Ayalew, D., Yirgu, G., Dell'Erba, F., Di Vito, M.A., Isaia, R., 2014. Genesis and evolution of mafic and felsic magmas at Quaternary volcanoes within the Main Ethiopian Rift: Insights from Gedemsa and Fanta 'Ale complexes. Lithos 188, 130–144. https://doi.org/10.1016/j.lithos.2013.08.008

Gíslason, G., Eysteinsson, H., Björnsson, G., Harðardóttir, V., 2015. Results of Surface Exploration in the Corbetti Geothermal Area, Ethiopia. World Geotherm. Congr. 2015 1–10.

Gleeson, M.L.M., Stock, M.J., Pyle, D.M., Mather, T.A., Hutchison, W., Yirgu, G., Wade, J., 2017. Constraining magma storage conditions at a restless volcano in the Main Ethiopian Rift using phase equilibria models. J. Volcanol. Geotherm. Res. 337, 44–61. https://doi.org/10.1016/j.jvolgeores.2017.02.026

Gottsmann, J., Biggs, J., Lloyd, R., Biranhu, Y., Lewi, E., 2020. Ductility and Compressibility Accommodate High Magma Flux Beneath a Silicic Continental Rift Caldera: Insights From Corbetti Caldera (Ethiopia). Geochem. Geophys. Geosystems 21. https://doi.org/10.1029/2020gc008952

Gualda, G.A.R., Ghiorso, M.S., Lemons, R.V., Carley, T.L., 2012. Rhyolite-MELTS: a Modified Calibration of MELTS Optimized for Silica-rich, Fluid-bearing Magmatic Systems. J. Petrol. 53, 875–890. https://doi.org/10.1093/petrology/egr080

Hughes, E.C., Neave, D.A., Dobson, K.J., Withers, P.J. and Edmonds, M., 2017. How to fragment peralkaline rhyolites: Observations on pumice using combined multi-scale 2D and 3D imaging. *Journal of Volcanology and Geothermal Research*, *336*, pp.179-191.

Hunt, J.A., Pyle, D.M., Mather, T.A., 2019. The geomorphology, structure, and lava flow dynamics of peralkaline rift volcanoes from high-resolution digital elevation models. Geochem. Geophys. Geosystems. https://doi.org/10.1029/2018GC008085

Hutchison, W., Fusillo, R., Pyle, D.M., Mather, T.A., Blundy, J.D., Biggs, J., Yirgu, G., Cohen, B.E., Brooker, R.A., Barfod, D.N., Calvert, A.T., 2016a. A pulse of mid-Pleistocene rift volcanism in Ethiopia at the dawn of modern humans. Nat. Commun. 7, 1–12. https://doi.org/10.1038/ncomms13192

Hutchison, W., Mather, T.A., Pyle, D.M., Boyce, A.J., Gleeson, M.L.M., Yirgu, G., Blundy, J.D., Ferguson, D.J., Vye-Brown, C., Millar, I.L., Sims, K.W.W., Finch, A.A., 2018. The evolution of magma during continental rifting: New constraints from the isotopic and trace element signatures of silicic magmas from Ethiopian volcanoes. Earth Planet. Sci. Lett. 489, 203–218. https://doi.org/10.1016/j.epsl.2018.02.027

Hutchison, W., Pyle, D.M., Mather, T.A., Yirgu, G., Biggs, J., Cohen, B.E., Barfod, D.N., Lewi, E., 2016b. The eruptive history and magmatic evolution of Aluto volcano: new insights into silicic peralkaline volcanism in the Ethiopian rift. J. Volcanol. Geotherm. Res. 328, 9–33. https://doi.org/10.1016/j.jvolgeores.2016.09.010

Iddon, F., Edmonds, M., 2020. Volatile-Rich Magmas Distributed Through the Upper Crust in the Main Ethiopian Rift. Geochem. Geophys. Geosystems 21. https://doi.org/10.1029/2019GC008904

Iddon, F., Jackson, C., Hutchison, W., Fontijn, K., Pyle, D.M., Mather, T.A., Yirgu, G., Edmonds, M., 2019. Mixing and Crystal Scavenging in the Main Ethiopian Rift Revealed by Trace Element Systematics in Feldspars and Glasses. Geochem. Geophys. Geosystems 20, 230–259. https://doi.org/10.1029/2018GC007836

Jorgenson, C., Higgins, O., Petrelli, M., Bégué, F., Caricchi, L., 2022. A Machine Learning-Based Approach to Clinopyroxene Thermobarometry: Model Optimization and Distribution for Use in Earth Sciences. J. Geophys. Res. Solid Earth 127, e2021JB022904. https://doi.org/10.1029/2021JB022904

Koppers A. A. (2002). ArArCALC—software for $^{40}Ar/^{39}Ar$ age calculations. *Computers & Geosciences*, *28*, 605-619.

Kress, V.C., Carmichael, I.S.E., 1991. The compressibility of silicate liquids containing Fe_2O_3 and the effect of composition, temperature, oxygen fugacity and pressure on their redox states. Contrib. Mineral. Petrol. 108, 82–92. https://doi.org/10.1007/BF00307328

Lee, J.Y., Marti, K., Severinghaus, J.P., Kawamura, K., Yoo, H.S., Lee, J.B., Kim, J.S., 2006. A redetermination of the isotopic abundances of atmospheric Ar. *Geochim. Cosmochim. Acta* **70** (17), 4507-4512. https://doi.org/10.1016/j.gca.2006.06.1563.

Lloyd, R., Biggs, J., Birhanu, Y., Wilks, M., Gottsmann, J., Kendall, M.J., Ayele, A., Lewi, E., Eysteinsson, H., 2018a. Sustained Uplift at a Continental Rift Caldera. J. Geophys. Res. Solid Earth 123, 5209–5226. https://doi.org/10.1029/2018JB015711

Lloyd, Ryan, Biggs, J., Wilks, M., Nowacki, A., Kendall, J.M., Ayele, A., Lewi, E., Eysteinsson, H., 2018b. Evidence for cross rift structural controls on deformation and seismicity at a continental rift caldera. Earth Planet. Sci. Lett. 487, 190–200. https://doi.org/10.1016/j.epsl.2018.01.037

Macdonald, R., White, J.C., Belkin, H.E., 2021. Peralkaline silicic extrusive rocks: magma genesis, evolution, plumbing systems and eruption. Comptes Rendus - Geosci. 353, 7–59. https://doi.org/10.5802/crgeos.97

Martin-Jones, C.M., Lane, C.S., Pearce, N.J.G., Smith, V.C., Lamb, H.F., Schaebitz, F., Viehberg, F., Brown, M.C., Frank, U., Asrat, A., 2017. Recurrent explosive eruptions from a high-risk Main Ethiopian Rift volcano throughout the Holocene. Geology 45, 1127–1130. https://doi.org/10.1130/G39594.1

McDonough, W.F., Sun, S. -s., 1995. The composition of the Earth. Chem. Geol., Chemical Evolution of the Mantle 120, 223–253. https://doi.org/10.1016/0009-2541(94)00140-4

Mollo, S., Masotta, M., Forni, F., Bachmann, O., De Astis, G., Moore, G., Scarlato, P., 2015. A K-feldspar–liquid hygrometer specific to alkaline differentiated magmas. Chem. Geol. 392, 1–8. https://doi.org/10.1016/j.chemgeo.2014.11.010

Neave, D.A., Fabbro, G., Herd, R.A., Petrone, C.M., Edmonds, M., 2012. Melting, differentiation and degassing at the pantelleria volcano, Italy. J. Petrol. 53, 637–663. https://doi.org/10.1093/petrology/egr074

Niespolo E. M., Rutte D., Deino A. L., Renne P. R. (2017). Intercalibration and age of the Alder Creek sanidine $^{40}Ar/^{39}Ar$ standard. *Quaternary Geochronology*, *39*, 205-213.

Peccerillo, A., Barberio, M.R., Yirgu, G., Ayalew, D., Barbieri, M., Wu, T.W., 2003. Relationships between Mafic and Peralkaline Silicic Magmatism in Continental Rift Settings: a Petrological, Geochemical and Isotopic Study of the Gedemsa Volcano, Central Ethiopian Rift. J. Petrol. 44, 2003–2032. https://doi.org/10.1093/petrology/egg068

Peccerillo, A., Donati, C., Santo, A.P., Orlando, A., Yirgu, G., Ayalew, D., 2007. Petrogenesis of silicic peralkaline rocks in the Ethiopian rift: Geochemical evidence and volcanological implications. J. Afr. Earth Sci. 48, 161–173. https://doi.org/10.1016/j.jafrearsci.2006.06.010

Peccerillo, A., Mandefro, B., Solomon, G., Bedru, H., Tesfaye, K., 1998. The Precambrian rocks from Southern Ethiopia: petrology, geochemistry and their interaction with the Recent volcanism from the Ethiopian Rift Valley. Neues Jahrb. Für Mineral. - Abh. 237–262. https://doi.org/10.1127/NJMA/173/1998/237

Putirka, K.D., 2008. Thermometers and barometers for volcanic systems. Rev. Mineral. Geochem. 69, 61–120. https://doi.org/10.2138/rmg.2008.69.3

Rapprich, V., Žáček, V., Verner, K., Erban, V., Goslar, T., Bekele, Y., Legesa, F., Hroch, T., Hejtmánková, P., 2016. Wendo Koshe Pumice: The latest Holocene silicic explosive eruption product of the Corbetti Volcanic System (Southern Ethiopia). J. Volcanol. Geotherm. Res. 310, 159–171. https://doi.org/10.1016/j.jvolgeores.2015.12.008

Roeder, P.L., Emslie, R.F., 1970. Olivine-Liquid Equilibrium. Contrib. Mineral. Petrol. 29, 275–289.

Renne P. R., Balco G., Ludwig K. R., Mundil R., Min K. (2011). Response to the comment by WH Schwarz et al. on "Joint determination of 40 K decay constants and $^{40}Ar*/^{40}K$ for the Fish Canyon sanidine standard, and improved accuracy for $^{40}Ar/^{39}Ar$ geochronology" by PR Renne et al. (2010). *Geochimica et Cosmochimica Acta*, *75*, 5097-5100.

Romano, P., Scaillet, B., White, J.C., Andújar, J., Di Carlo, I., Rotolo, S.G., 2020. Experimental and thermodynamic constraints on mineral equilibrium in pantelleritic magmas. Lithos 376–377. https://doi.org/10.1016/j.lithos.2020.105793

Ronga, F., Lustrino, M., Marzoli, A., Melluso, L., 2009. Petrogenesis of a basalt-comendite-pantellerite rock suite: The Boseti Volcanic Complex (Main Ethiopian Rift). Mineral. Petrol. 98, 227–243. https://doi.org/10.1007/s00710-009-0064-3

Rooney, T., Furman, T., Bastow, I., Ayalew, D., Yirgu, G., 2007. Lithospheric modification during crustal extension in the Main Ethiopian Rift. J. Geophys. Res. Solid Earth 112. https://doi.org/10.1029/2006JB004916

Rooney, T.O., Hart, W.K., Hall, C.M., Ayalew, D., Ghiorso, M.S., Hidalgo, P., Yirgu, G., 2012. Peralkaline magma evolution and the tephra record in the Ethiopian Rift. Contrib. Mineral. Petrol. 164, 407–426. https://doi.org/10.1007/s00410-012-0744-6

Samrock, F., Grayver, A.V., Bachmann, O., Karakas, Ö., Saar, 2021. Integrated magnetotelluric and petrological analysis of felsic magma reservoirs: Insights from Ethiopian rift volcanoes. Earth Planet. Sci. Lett. 559, 116765. https://doi.org/10.1016/j.epsl.2021.116765

Scaillet, B., MacDonald, R., 2003. Experimental constraints on the relationships between peralkaline rhyolites of the Kenya Rift Valley. J. Petrol. 44, 1867–1894. https://doi.org/10.1093/petrology/egg062

Scaillet, B., Macdonald, R., 2001. Phase Relations of Peralkaline Silicic Magmas and Petrogenetic Implications. J. Petrol. 42, 825–845. https://doi.org/10.1093/petrology/42.4.825

Shand, S.J., 1927. On the Relations between Silica, Alumina, and the Bases in Eruptive Rocks, considered as a Means of Classification. Geol. Mag. 64, 446–449. https://doi.org/10.1017/S0016756800103760

Suikkanen, E., 2020. easyMelts-GUI [WWW Document]. Magma Source. URL https://magmasource.caltech.edu/gitlist/easyMelts.git/tree/master/ (accessed 3.14.23).

Tadesse, A.Z., Ayalew, D., Pik, R., Yirgu, G., Fontijn, K., 2019. Magmatic evolution of the Boku Volcanic Complex, Main Ethiopian Rift. J. Afr. Earth Sci. 149, 109–130. https://doi.org/10.1016/j.jafrearsci.2018.08.003

Tadesse, A.Z., Fontijn, K., Caricchi, L., Bégué, F., Gudbrandsson, S., Smith, V.C., Gopon, P., Debaille, V., Laha, P., Terryn, H., Yirgu, G., Ayalew, D., 2023. Pre-eruptive storage conditions and magmatic evolution of the Bora-Baricha-Tullu Moye volcanic system, Main Ethiopian Rift. Lithos 442–443, 107088. https://doi.org/10.1016/j.lithos.2023.107088

Tadesse, A.Z., Fontijn, K., Melaku, A.A., Gebru, E.F., Smith, V.C., Tomlinson, E., Barfod, D., Gopon, P., Bégué, F., Caricchi, L., Laha, P., Terryn, H., Gudbrandsson, S., Yirgu, G., Ayalew, D., 2022. Eruption frequency and magnitude in a geothermally active continental rift: The Bora-

Baricha-Tullu Moye volcanic complex, Main Ethiopian Rift. J. Volcanol. Geotherm. Res. 107471. https://doi.org/10.1016/j.jvolgeores.2022.107471

Teklemariam, M., Battaglia, S., Gianelli, G., Ruggieri, G., 1996. Hydrothermal alteration in the Aluto-Langano geothermal field, Ethiopia. Geothermics 25, 679–702. https://doi.org/10.1016/S0375-6505(96)00019-3

Vidal, C.M., Lane, C.S., Asrat, A., Barfod, D.N., Mark, D.F., Tomlinson, E.L., Tadesse, A.Z., Yirgu, G., Deino, A., Hutchison, W., Mounier, A., Oppenheimer, C., 2022, Age of the oldest known Homo sapiens from eastern Africa. Nature. https://doi.org/10.1038/s41586-021-04275-8

Waters, L., Lange, R., 2015. An updated calibration of the plagioclase-liquid hygrometer-thermometer applicable to basalts through rhyolites. Am. Mineral. 100, 2172–2184. https://doi.org/10.2138/am-2015-5232

Weis, D., Kieffer, B., Maerschalk, C., Barling, J., de Jong, J., Williams, G.A., Hanano, D., Pretorius, W., Mattielli, N., Scoates, J.S., Goolaerts, A., Friedman, R.M., Mahoney, J.B., 2006. High-precision isotopic characterization of USGS reference materials by TIMS and MC-ICP-MS. Geochem. Geophys. Geosystems 7. https://doi.org/10.1029/2006GC001283

White, J.C., Macdonald, R., Bagiński, B., Liszewska, K.M., 2023. Extreme differentiation along multiple liquid lines of descent in strongly peralkaline magma series at Pantelleria (Italy). J. Petrol. egad001. https://doi.org/10.1093/petrology/egad001

White, J.C., Parker, D.F., Ren, M., 2009. The origin of trachyte and pantellerite from Pantelleria, Italy: Insights from major element, trace element, and thermodynamic modelling. J. Volcanol. Geotherm. Res. 179, 33–55. https://doi.org/10.1016/j.jvolgeores.2008.10.007

Whitney, D.L., Evans, B.W., 2010. Abbreviations for names of rock-forming minerals. Am. Mineral. 95, 185–187. https://doi.org/10.2138/am.2010.3371

Wieser, P.E., Petrelli, M., Lubbers, J., Wieser, E., Kent, A., 2021. Thermobar : An Open-Source Python3 tool for Thermobarometry and Hygrometry. Volcanica.

Wilks, M., Ayele, A., Kendall, J.-M., Wookey, J., 2017. The 24th January 2016 Hawassa earthquake: Implications for seismic hazard in the Main Ethiopian Rift. J. Afr. Earth Sci. 125, 118–125. https://doi.org/10.1016/j.jafrearsci.2016.11.007

Wong, K., Ferguson, D., Matthews, S., Morgan, D., Tadesse, A.Z., Sinetebeb, Y., Yirgu, G., 2022. Exploring rift geodynamics in Ethiopia through olivine-spinel Al-exchange thermometry and rare-earth element distributions. Earth Planet. Sci. Lett. 597, 117820. https://doi.org/10.1016/j.epsl.2022.117820

Authors statement CRediT

David J Colby: Conceptualization, Investigation, Formal analysis, Writing - Original Draft, Writing - Review & Editing, Project administration, Visualization.

David M Pyle: Conceptualization, Writing - Review & Editing, Supervision, Project administration.

Karen Fontijn: Conceptualization, Writing - Review & Editing, Supervision, Resources, Project administration

Tamsin A Mather: Conceptualization, Writing - Review & Editing, Supervision, Project administration, Funding acquisition.

Sebastien Nomade: Writing - Review & Editing, Formal analysis, Investigation

Abate A Melaku: Writing - Review & Editing, Project administration.

Million A Megesha: Writing - Review & Editing, Project administration.

Gezahegn Yirgu: Conceptualization, Writing - Review & Editing, Project administration.

Declaration of interests

☒The authors declare that they have no known competing financial interests or personal relationships that could have appeared to influence the work reported in this paper.

☐The authors declare the following financial interests/personal relationships which may be considered as potential competing interests:

Highlights

- We present new data from the only known basaltic units within Corbetti Caldera.
- We determine shallow magma storage conditions between 100-250 MPa at temperatures ~1100 ºC for the basaltic magma and ~793 ºC for the peralkaline magma.
- Corbetti's magmas are hydrous with ~ 5.5 wt.% H_2O.
- We date a pre-caldera lava flow to ~207 ka and a post-caldera ignimbrite to 160 ka